Catalytic pyrolysis of plastic waste using metal-incorporated activated carbons for monomer recovery and carbon nanotube synthesis

Gerardo Martínez-Narro[a], Ha H. Phan[a], Samaila Hassan[a], Simon K. Beaumont[b], Anh N. Phan[a*]

[a]*School of Engineering, Newcastle University, Newcastle upon Tyne, NE1 7RU, United Kingdom*

[b]*Department of Chemistry, Durham University, South Road, Durham DH1 3LE, U.K.*

[*]anh.phan@newcastle.ac.uk

Abstract

As the global plastic waste crisis intensifies, innovative and sustainable solutions are urgently needed. This study evaluated waste-derived metal-incorporated activated carbon (AC) catalysts for the pyrolysis of mixed plastic waste to generate value-added products, focusing on product yield distribution, composition, hydrogen, and carbon nanotube (CNT) formation. Pyrolysis-catalysis experiments were conducted using a two-stage fixed-bed reactor, wherein the temperature was maintained at 500 °C in first stage (pyrolysis) and varied (500, 600, and 700 °C) in the second stage (catalysis). The tested ACs were incorporated with nickel (Ni-AC), iron (Fe-AC), and zinc (Zn-AC) to assess the impact of metal particles distributed on the carbonaceous support in the second stage. The results from the ACs were compared to those obtained using zeolite (H-ZSM-5), Raw-AC, and non-catalytic runs. The Ni-AC and Fe-AC demonstrated superior catalytic activity, with Ni-AC being more efficient in producing hydrogen (4.24 wt%) and CNTs (34.5 wt%) with diameters of approximately 30 nm, and Fe-AC leading to higher gas yields (68.8 wt%) and CNTs (12.4 wt%) of around 60 nm. In contrast, Zn-AC and Raw-AC presented limited effectiveness, although Raw-AC moderately outperformed Zn-AC with enhanced gas yields and reduced oil/wax yields. The zeolite H-ZSM-5 exhibited the highest gas yields (78 wt%), converting heavy fractions into lighter molecules, notably the monomers ethylene and propylene. These findings provide valuable insights into catalyst selection and optimization for plastic waste pyrolysis processes, with H-ZSM-5 being the most effective catalyst for monomer recovery, and Ni-AC and Fe-AC demonstrating promising results.

Keywords: chemical recycling, biochar, hydrogen, sustainability, circularity

1. Introduction

Due to their durability and versatility, plastic products have become an integral part of everyday life. However, the same characteristics that make plastics so useful also contribute to a mounting global waste crisis. Mismanaged plastic waste poses substantial threats to terrestrial and aquatic ecosystems, and current waste management practices such as landfilling, and incineration have significant environmental and health repercussions [1, 2]. Despite widespread recycling efforts, only a small fraction (approximately 32%) of plastic waste is currently recycled effectively, while the vast majority is destined to landfills or

incineration [3]. Therefore, innovative alternative methods to manage plastic waste in a more sustainable way are necessary.

The field of plastic waste management is undergoing a transformative change, thanks to the integration of technologies such as cold plasma-assisted pyrolysis (CPAP), microwave-assisted pyrolysis (MAP), hydrothermal processing (HTP), selective solvolysis (SS), and advancements in biological treatments, mechanical recycling, and artificial intelligence. CPAP is regarded for its energy efficiency and enhanced chemical selectivity under a highly reactive environment at low temperatures [4, 5]. MAP stands out for its rapid and selective heating, optimizing energy consumption and offering adaptability for various plastic waste types [6, 7]. HTP and SS allow the recovery of monomers for the subsequent manufacture of new plastics [8-10]. In addition, breakthroughs in enzyme engineering, like the creation of more potent PET-degrading enzymes, are speeding up the biological decomposition of plastics [11]. AI and robotics are being enhanced to improve sorting efficiency, ensuring that plastics are effectively separated for recycling [12, 13].

Waste-derived materials, such as biochar and activated carbon, have been increasingly recognized as potential catalysts for the pyrolysis of plastic waste [14-16]. Their use not only reduces waste but also provides an economically viable option for sustainable waste management, as these materials can be obtained at lower costs than other widely used catalysts such as commercial zeolites [17].

Activated carbons usually present a hierarchical structure due to their wide distribution of pore sizes [18]. The use of catalysts with this structure has several advantages for the pyrolysis of plastic waste, such as the potential to improve the efficiency and selectivity of the process through multiple approaches [19]. One of the most notable benefits of hierarchical catalysts is the enhanced accessibility they provide. Since the bulky nature of the plastic can lead to steric hindrances or diffusion constraints, the presence of micropores, mesopores, and macropores within a hierarchical catalyst ensures that plastic waste can readily access the catalyst's active sites [20]. Micropores contribute to the adsorption and desorption of reactants and products, while mesopores facilitate efficient mass transport and diffusion. Macropores, on the other hand, aid in preventing pore blockage and promoting bulk transport [21]. The multilevel pore structure significantly enhances the accessibility of pyrolytic volatiles to the catalytic sites, thereby improving the overall reaction rate [22]. Moreover, the

hierarchical pore structure permits improved mass transport of reactants and products throughout the catalyst. The interconnected network of pores enables the diffusion of large molecules to the internal active sites, and the efficient removal of reaction products [23]. This minimizes diffusional limitations and prevents pore blockage, leading to a more effective pyrolysis process. The role of support materials in determining catalyst properties is essential, since they aid in the dissemination of active metal particles, enabling improved mass transport and providing a suitable environment for chemical reactions to occur, owing to their unique physical and chemical structure [24].

Johar et al. [25] designed a biologically nickel-bound biochar catalyst for the depolymerization of polyethylene into high-value chemicals via microwave-assisted pyrolysis. This catalyst effectively enhanced the production of C_6-C_{12} aliphatics, dehydrocyclization of linear alkanes, and H_2 release as gaseous fraction. Wang et al. [26] employed nanocellulose-derived biochar as a catalyst for pyrolyzing low-density polyethylene (LDPE) into hydrogen and liquid fuels. The study revealed that at 500 °C and a biochar to LDPE ratio of >3, the plastic could be completely degraded into liquid and gas without wax formation. Moreover, the biochar catalyst proved efficient in converting real waste plastics (e.g., grocery bags and packaging trays) into valuable liquid and H_2-enriched gas products. In a separate study [27], biochars derived from agricultural waste (corn stover and Douglas fir) were utilized for the pyrolysis of waste plastics (i.e., PS, PET, PP, LDPE, and HDPE). The corn stover biochar, which resulted in a liquid yield of approximately 40 wt%, without wax formation, generated 60-80 vol% of H2 in the gas yield, and exhibited high activity after 20 cycles of reuse. Similarly, Park et al. [28] examined the application of nickel-incorporated lignin-derived biochar for HDPE gasification. The biochar catalyst demonstrated high H_2 yields (0.093 $mmolH_2\ g^{-1}_{plastic}$) from the gasification process, which was attributed to the high dispersion/distribution of Ni on the biochar. The study concludes that Ni supported on char could be an economically feasible catalyst for producing hydrogen from gasification of plastics.

The plastic waste pyrolysis products are diverse and valuable, including light oil (naphtha), hydrogen, CNTs, and monomers. CNTs have a wide range of applications in various fields such as electronics, energy storage, and materials science [29, 30]. Recent studies have shown that CNTs can be produced from plastic waste pyrolysis, and the quality and quantity of CNTs can be controlled by adjusting the pyrolysis conditions and the type of catalyst used [31].

Monomers, as the building blocks of polymers, are another valuable product that can be obtained from plastic waste. For example, up to 50 wt.% ethylene monomers can be recovered from polyethylene waste through pyrolysis, albeit at high temperatures (1000 °C) [32].

This study is motivated by the need to overcome the limitations present in existing plastic waste recycling approaches and aims to explore effective alternatives. A noticeable gap exists in literature regarding the performance differentiation of various metal-incorporated activated carbons in plastic pyrolysis [26, 27, 33]. Research deficiency in the investigation of activated carbon catalytic pyrolysis of plastics highlights the need for comprehensive studies focused on understanding the catalytic pyrolysis process. Additionally, lack of in-depth exploration into the mechanisms governing the selectivity among various catalysts in the production of hydrogen, carbon nanotubes, and monomers also underscores a knowledge gap that is crucial for enhancing the efficiency and selectivity of catalytic pyrolysis processes, contributing to the production of valuable by-products. Moreover, an underexplored area is the impact of distinct catalyst bed temperatures within two-stage reactors, where initial pyrolysis and catalysis-driven processes are spatially segregated. Our focus is on the catalytic pyrolysis process, a promising strategy for alleviating plastic waste issues while simultaneously enabling the extraction of valuable chemical derivatives. We delve into an in-depth analysis of Ni, Fe, and Zn-loaded activated carbons as catalysts, aiming to evaluate their efficacy in augmenting plastic waste recycling efficiency and their selectivity in producing hydrogen, carbon nanotubes, and monomers. Emphasis is placed on assessing the interplay of temperature variations and distinct catalysts on the yields and compositions of oil, gas, char, and carbon deposition. This inquiry, rooted in the application of waste-derived catalysts in plastic waste pyrolysis, aspires to enhance the eco-friendliness of recycling processes and underscores the viability of these catalysts as substitutes for traditional materials.

2. Materials and methods

2.1. Plastic waste

Plastic waste samples, consisting of HDPE, LDPE, PP, PS, and PET, were obtained from Byker Household Waste Recycling Centre in Newcastle upon Tyne. Each type of plastic was isolated, washed, dried, and cut into 1 mm^2 squared pieces. Proximate analysis, following the British

131 standard BS-1016-3, was conducted to determine the moisture, ash, volatile matter, and fixed
132 carbon content of the samples. Elemental analysis was conducted using a CHN628 Series
133 Elemental Determinator at the Advanced Chemical and Materials Analysis (ACMA) unit at
134 Newcastle University. The results, presented in Table 1, indicate that the samples consisted
135 primarily of volatile matter (95.4 wt%), with low levels of ash (2.37 wt%) and negligible
136 moisture (0.15 wt%). The most abundant elements in the plastic samples are C and H, while
137 the oxygen content is minimal for all plastics, except for PET. For every pyrolysis run,
138 simulated mixtures were prepared based on the reported composition of global primary
139 plastic waste generation (i.e., 20% HDPE, 28.5% LDPE, 27.5 PP, 9% PS, and 15% PET) [34].

140 Table 1. Proximate analysis (as received), and elemental analysis (dry ash-free basis) of plastic
141 waste samples (wt%). Error bars are based on the standard deviation of measurements
142 conducted in triplicate.

Sample	Moisture	Ash	Fixed Carbon	Volatile matter	C	H	N	O[a]
PP	0.15 ± 0.04	2.18 ± 0.12	0.21 ± 0.07	97.61 ± 0.38	84.89	13.91	0.21	0.99
LDPE	0.17 ± 0.08	6.12 ± 0.29	0.60 ± 0.25	93.28 ± 2.12	84.66	14.24	0.43	0.67
PET	0.26 ± 0.13	0.70 ± 0.1	8.28 ± 1.74	91.03 ± 0.41	62.56	4.28	0.12	33.04
HDPE	0.04 ± 0.03	0.14 ± 0.06	0.22 ± 0.09	99.64 ± 0.52	86.02	13.82	0.02	0.14
PS	0.12 ± 0.07	2.43 ± 0.08	2.36 ± 1.18	95.21 ± 1.19	91.79	7.67	0.09	0.45

143 [a] by difference.

144 *2.2. Catalyst preparation and characterisation*

145 The activated carbon (AC) was produced in-house by subjecting walnut shells to heat
146 treatment at a temperature of 700 °C in the presence of flowing CO_2 for 1 h. The selection of
147 these conditions was based on their previous demonstration of generating ACs possessing
148 high porosity and high surface area [35]. After the reaction, the AC was pulverized using a

mortar and subsequently sifted to obtain a fine powder with a diameter of approximately 50 µm.

For metal loading, nickel was chosen due to its outstanding catalytic properties, which enhance the cleavage of plastic waste C-C bonds, promote the decomposition of long-chain hydrocarbons, and provide high selectivity for H_2 and CNTs [36]. Nickel particles act as active sites for catalytic reactions, while the highly porous structure of AC offers a substantial surface area for both the dispersion of nickel and the adsorption and subsequent dissociation of hydrocarbon molecules [37]. Similar to the catalytic effect of nickel, the active sites of iron catalysts promote the cleavage of C-C and C-H bonds in the long-chain plastic molecules, which facilitates their conversion into smaller products [38]. Zinc has been shown to have catalytic properties that are beneficial to plastic waste pyrolysis, such as enhances gas yields compared to non-catalytic pyrolysis, and the improved quality of oils [39].

The wet impregnation method was used for metal incorporation. A 100 mL solution containing either nickel nitrate hexahydrate, iron (III) nitrate nonahydrate, or zinc nitrate hexahydrate (Sigma Aldrich) was prepared and combined with raw AC. The proportions of nitrate salts and AC were determined to achieve a 2:1 mass ratio of AC to the resulting metal oxide after calcination. The resulting slurries were vigorously stirred for 12 h at 60 °C, then dried in an oven at 105 °C for 12 h, calcined at 600 °C in a flow of nitrogen (100 ml min^{-1}) for 4 h, and finally ground and sieved into fine particles of around 50 µm diameter. The H-ZSM-5 zeolite (312 SiO_2/Al_2O_3 molar ratio, 413 m^2 g^{-1} surface area) was calcinated in static air at 550 °C for 4 h at a heating rate of 20 °C min^{-1}.

The composition and structure of the catalysts were analysed through Scanning Electron Microscopy (SEM), Energy-dispersive X-ray spectroscopy (EDX), and X-ray diffraction (XRD). SEM images and EDX elemental mapping were obtained in a JEOL JSM-5610LV SEM operating at low vacuum and coupled with an energy dispersive X-ray spectroscopy (EDX) module. The analyses were conducted on uncoated samples mounted on standard SEM stubs.

XRD analysis was performed in a PANalytical X'Pert Pro MPD with Xcelerator detector using Cu Kα radiation.

The micropore volume and surface area of the AC samples and zeolite were evaluated by CO_2 adsorption at a temperature of 0 °C by means of an Hiden Isochema Intelligent Gravimetric

Analyser (IGA). Isotherms were recorded at each pressure point (0-100 kPa) in an ultrahigh vacuum system. Prior to each run, 50 mg of the AC sample was degassed at 120 °C overnight under vacuum (<10^{-6} Pa) for all moisture to be removed until achieving a constant weight before a static gas sorption/desorption isotherm was recorded. The CO_2 adsorption-desorption isotherm was analysed using the Dubinin-Radushkevich (DR) model. The mesopore volume and surface area of the samples were evaluated by N_2 physisorption isotherms at 77 K using a Micromeritics TriStar II Plus and Brunauer-Emmett-Teller (BET) equation with samples dried at 105 °C overnight and outgassed at 350 °C at high vacuum for 24 h prior to analysis.

2.3. Pyrolysis setup

The experimental configuration involved a two-stage fixed-bed stainless steel reactor (1.25 in diameter, and 17 in length) fitted with two heating bands (spaced 5.1 in apart) for independently controlled temperatures for the two zones. The outlet of the reactor was connected to the condensers cooled at -13 °C using a saturated frigorific solution of salt and ice water as illustrated in Figure 4. Before initiating the experiments, the reactor was purged with N_2 for 30 min to ensure the system is air-free (verified by GC analysis). Following this, the first reactor stage (pyrolysis section), holding 3 g of plastic mixture was heated at a rate of 20 °C min^{-1} and sustained at 500 °C for 40 min at a fixed N_2 carrier gas flow rate of 40 ml min^{-1}. Quartz wool and a metallic mesh support which held 0.5 g of catalyst (i.e., 1:6 plastic-to-catalyst ratio) were placed in the second stage where the temperature was varied (500 – 700 °C). During the non-catalytic pyrolysis experiments, only quartz wool was in place with no catalyst. Non-condensable gases were collected at the outlet of the condenser system using multiple Tedlar gas bags and the entirety of the gas products were collected. The mass differences in the crucible, condensers, and catalyst bed pre- and post-reaction were employed to calculate the masses of the produced char, oil, and catalyst carbon deposition, respectively. In cases where carbon nanotubes were detected, carbon deposition was referred to as CNT, and their masses were calculated by subtracting the mass of carbon deposition on Raw-AC from the masses observed on Ni-AC and Fe-AC at each respective temperature. The total mass of gaseous products was determined using gas chromatography, considering the known N_2 flow rate, collection time, and mol% of the samples. Equation 1 describes the mass balance:

$$M_{plastic} = M_{products} = M_{oil} + M_{gas} + M_{char} + M_{C\ deposition} \quad (1)$$

Where M stands for mass. The product yields were then calculated by equation 2:

$$Y_i = 100\left(\frac{M_i}{M_{plastic}}\right) \quad (2)$$

Where Y is the yield (wt%), and the subscript *i* denotes the type of product (oil, gas, char, and carbon deposition. All yields reported in this study are referred to the initial mass of plastic waste. Non-catalytic pyrolysis at 600 °C was conducted in triplicate to test reproducibility and the experimental errors on product yields and compositions were extrapolated to all tested conditions.

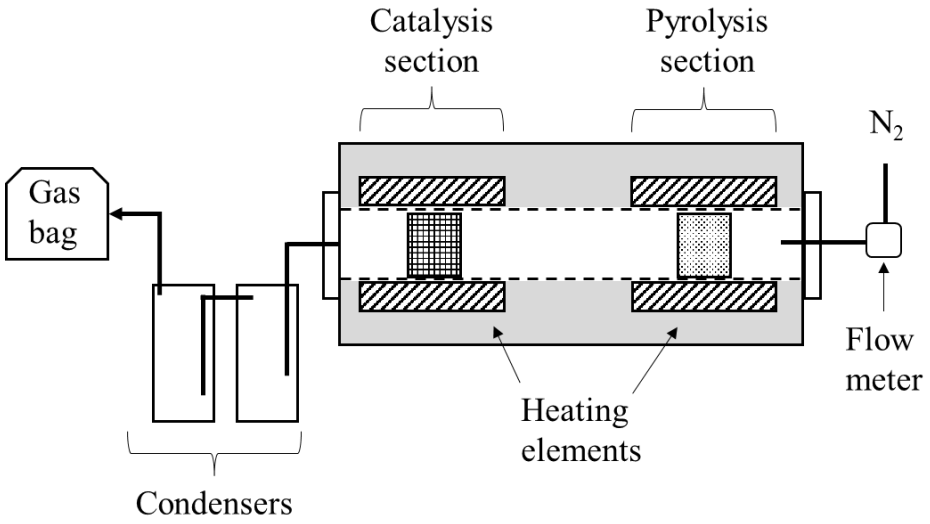

Figure 4. Schematic diagram of the pyrolysis-catalysis reactor and condensation system.

2.4. Product analysis

Non-condensable gases were collected for a total of 50 min and analysed offline using a Varian 450 gas chromatography equipped with both TCD and FID detectors. These detectors enabled the concurrent analysis of permanent gases (e.g., H_2, N_2, O_2, and CO), CO_2, and hydrocarbons (C1 – C4). The TCD inlet, detector, and oven temperatures were regulated at 250 °C, 175 °C, and 175 °C, respectively. Three columns were integrated into the GC, specifically a Hayesep T ultimetal, a Hayesep Q ultimetal, and a Molecular Sieve 13X. The gas specimen from the TCD detector was subsequently conducted into an Rt-Alumina BOND/MAPD column (30 m x 0.32 mm x 5 µm) connected to the FID detector, which was adjusted to 255 °C. The column was situated in an isolated oven with a programmed temperature sequence: Initially stabilized at 40 °C for 2 min, incrementally raised to 50 °C at

a rate of 4 °C min^{-1}, maintained for 0.5 min, then escalated to 80 °C at 8 °C min^{-1}, and finally increased to 145 °C at 20 °C min^{-1}.

Liquid products collected from the condensers after the system cooled down were dissolved in a 1:1 mixture of ethyl acetate and n-hexane and characterised using an Agilent 5977B MSD MS Single Quadrupole Mass Analyzer, linked to an Agilent 8890 Gas Chromatography system and utilizing an HP-5MS column (30 m x 0.25 mm x 0.25 µm). The inlet and detector temperatures were fixed at 280 °C, while the oven's temperature program commenced at 60 °C for 0.5 minutes, increased to 280 °C at a rate of 6.5 °C min^{-1}, and finally held at 280 °C for 13 min. For quantitative analysis, an Agilent 7820 Gas Chromatograph was employed, featuring an identical column and heating protocol as previously described. An internal standard (methyl stearate) and an external standard (C_7 – C_{40} saturated alkanes, Sigma Aldrich) were utilized for quantification purposes. The relative response factor (RRF) of each analyte was determined using known external and internal standard concentrations, and their peak area results via equation 3:

$$\frac{A_x}{C_x} = RRF\left(\frac{A_{is}}{C_{is}}\right) \quad (3)$$

Where A is the peak area, C is the concentration, and the subscripts “x” and “is” stand for analyte, and internal standard, respectively. The concentrations of the sample compounds were then calculated using their peak areas, the internal standard peak area, and the corresponding RRF according to equation 3. The masses of the sample compounds were then related to the initial plastic mass to determine their yields (wt%). For simplicity, hydrocarbons were categorized into three groups based on their carbon numbers <C_{10} (light), C_{10}-C_{18} (medium), and >C_{18} (heavy/wax) hydrocarbon fractions, respectively.

3. Results and discussion

3.1. Catalyst characterisation

In Figure 1 (a-b), the EDX elemental mapping shows that the metallic particles (highlighted in red/pink) were evenly dispersed across the AC catalyst surface. The macropore structure can be visualised in Figure 1 (c-f), this shape allows the bulky hydrocarbon volatiles to access the internal matrix of the catalyst more easily, where reaction occurs on the surface of the mesopores and micropores [40].

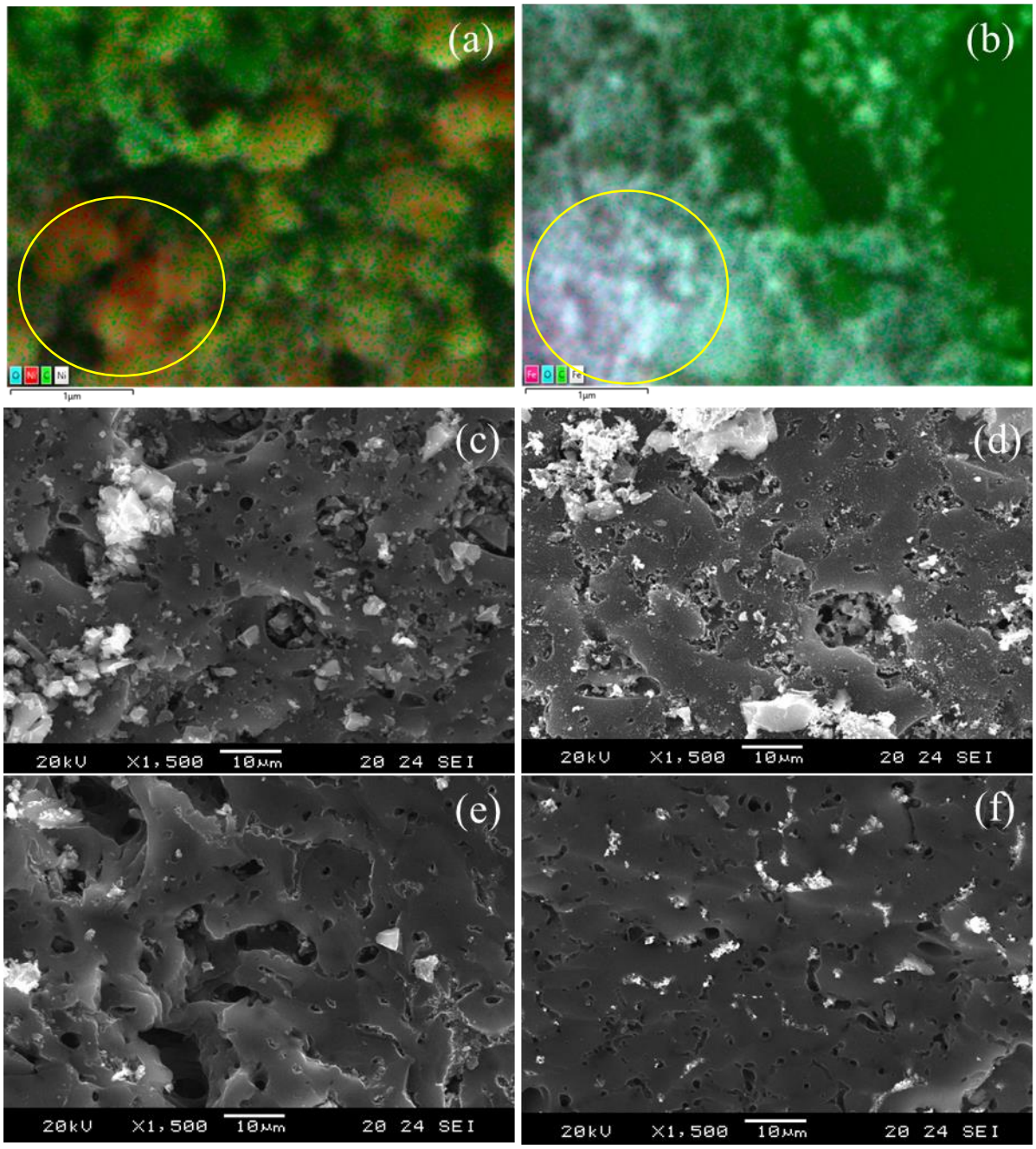

Figure 1. EDX mapping of nickel (a) and iron (b) incorporated AC, and SEM images of raw AC (c), nickel (d), iron (e), and zinc (f) incorporated AC.

Figure 2 illustrates the XRD patterns indicating the identified phases of raw and metal-incorporated AC catalysts.

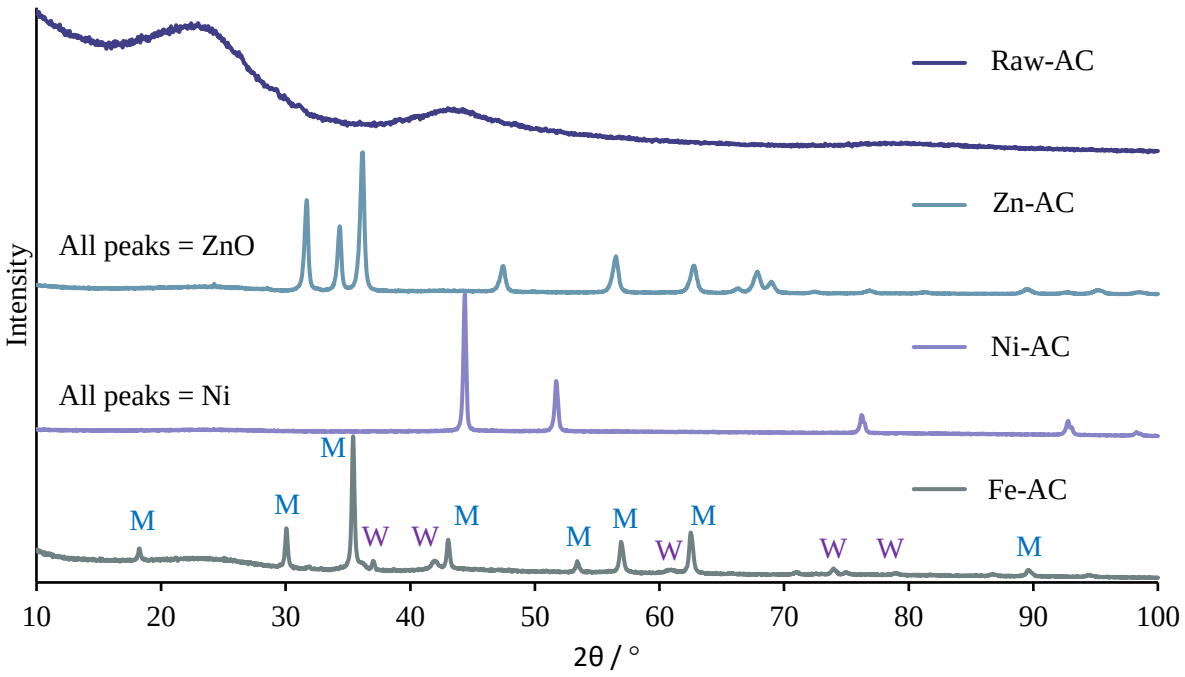

Figure 2. XRD spectra of AC catalysts (M = magnetite (Fe_3O_4), W = wuestite (FeO)).

The Raw-AC sample had insufficient peaks to determine its existing phases. Hexagonal ZnO was the only phase detected in Zn-AC, face-centred cubic nickel was the only phase of Ni-AC, and Fe-AC contained two forms of iron oxide: cubic Fe_3O_4 and FeO. Crystalline nickel oxide was absent, and only metallic nickel particles were detected. This characteristic in Ni-AC was examined via TG-MS analysis using a NETZSCH STA 449 F3 Jupiter fitted with QMS 403 Quadro/ Aëolos. The analysis was carried out within a helium environment, with temperatures varying between 35-700 °C at a heating rate of 10 °C min^{-1}. The range for mass measurement spanned from 10-150 m/z. As shown in Figure 3, the analysis indicates a series of mass losses, indicative of an interaction of nickel oxide and carbon in the catalyst support upon heating. This can result from the support reacting with the oxygen in NiO to release gaseous oxides. Between 150-300 °C, NO and/or NO_2 were detected, while CO and CO_2 were observed between 490-540 °C, confirming the reduction of nickel within the Ni-AC catalyst.

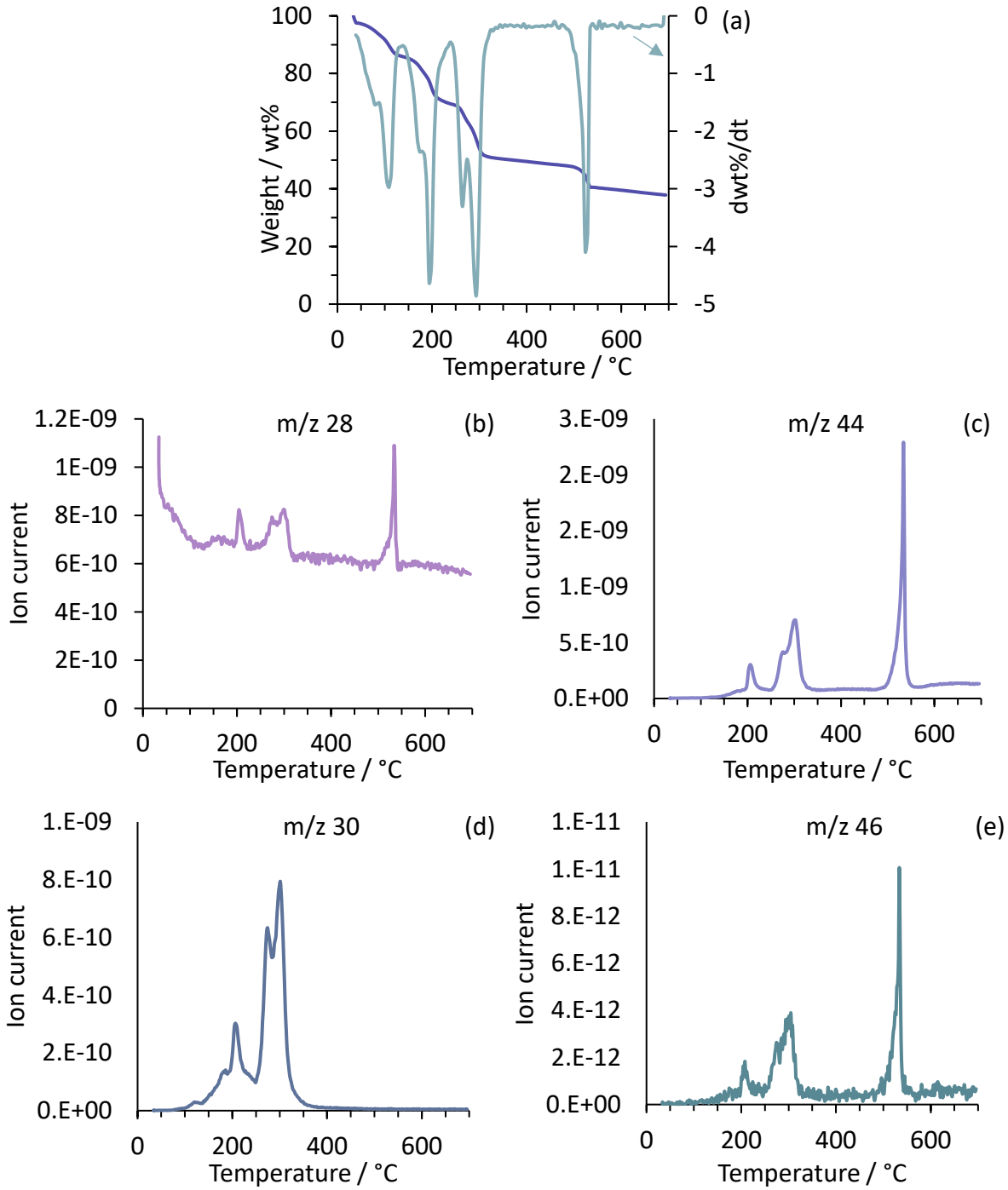

Figure 3. Ni-AC activation TGA results (a), MS results of m/z 28 (b), m/z 44 (c), m/z 30 (d), and m/z 46 (e).

Surface area and pore volume results are summarised in Table 2. As a result of biomass undergoing thermal processing with CO_2, the raw AC exhibits a highly porous structure with a micropore volume of 0.2055 $cm^3\ g^{-1}$ and a micropore surface area measuring 551.5 $m^2\ g^{-1}$. However, following the wet impregnation method, the overall surface area of the catalysts

decreased. The most notable reduction occurred in the Ni-AC, followed by Fe-AC, while the Fe-AC structure was the least affected by the metal impregnation procedure.

The isotherms of all catalysts (Figures S1-4) follow a Type I isotherm, indicating the domination of micropores in the carbon matrix. The micropore volume measured via N_2 adsorption ($V_{DR\ N2}$) of Raw-AC was 0.034 $cm^3\ g^{-1}$. This value is markedly lower than the volume determined through CO_2 adsorption (V_{CO2}), which was 0.2055 $cm^3\ g^{-1}$. This indicates the activated diffusion effect of N_2 at cryogenic temperatures (-196 °C), which can be attributed to the exceedingly narrow pore structure of Raw-AC. Therefore, these constricted micropores may not contribute to the gas-solid reactions during pyrolysis. The $V_{DR\ N2}$ of Ni-AC was 0.123 $cm^3\ g^{-1}$, which is similar to the V_{CO2} 0.1259 $cm^3\ g^{-1}$. These are open micropores where gas can easily diffuse into for any gas-solid reactions. The similarity of V_{CO2} (0.1471 $cm^3\ g^{-1}$) and $V_{DR\ N2}$ (0.141 $cm^3\ g^{-1}$) in Zn-AC indicates the open micropore structure, where gases can easily diffuse into these micropores for reactions.

Table 2. Pore volume and surface area results of AC catalysts.

Catalyst	S_{BET}[a] / $m^2\ g^{-1}$	V_{total}[b] / $cm^3\ g^{-1}$	$V_{DR\ N2}$[c] / $cm^3\ g^{-1}$	V_{meso}[d] / $cm^3\ g^{-1}$	S_{CO2}[e] / $m^2\ g^{-1}$	V_{CO2}[f] / $cm^3\ g^{-1}$
Raw-AC	111.19	0.043	0.034	0.009	551	0.2055
Ni-AC	308.36	0.147	0.123	0.024	338	0.1259
Fe-AC	314.24	0.171	0.127	0.044	473	0.1763
Zn-AC	351.88	0.174	0.141	0.033	395	0.1471

[a] S_{BET} = Surface area of carbon measured from N_2 adsorption at -196°C; [b] V_{total} = Total pore volume measured from N_2 adsorption -196 °C, at p/p_0 = 0.995; [c] $V_{DR\ N2}$ = Micropore volume measured from N_2 adsorption at -196°C at p/p_0 = 0.001-0.1; [d] Vmeso = Mesopore volume calculated from $V_{meso} = V_{total} - V_{DR\ N2}$; [e] V_{CO2} = Micropore volume measured from CO_2 adsorption at 0°C; [f] S_{CO2} = micropore surface area from CO_2 adsorption at 0°C.

3.2. Non-catalytic pyrolysis

Pyrolysis in the absence of catalyst was carried out at temperatures of 500, 600, and 700 °C in the second stage of the reactor to establish a baseline for examining the impact of catalysts on product yields and compositions. Product yields and compositions are shown in Figure 5. A summary of non-catalytic pyrolysis product yields in literature and this study is presented in Table 3. The variations in product yields and compositions observed in these studies can be

attributed to several factors such as the reactor configuration, types of plastic waste and their contaminants, which vary between the samples used by different researchers. Broadly speaking, however, similar trends in product distribution and a shift to lighter hydrocarbon products at higher temperatures were seen in both the current and literature non-catalytic pyrolysis studies.

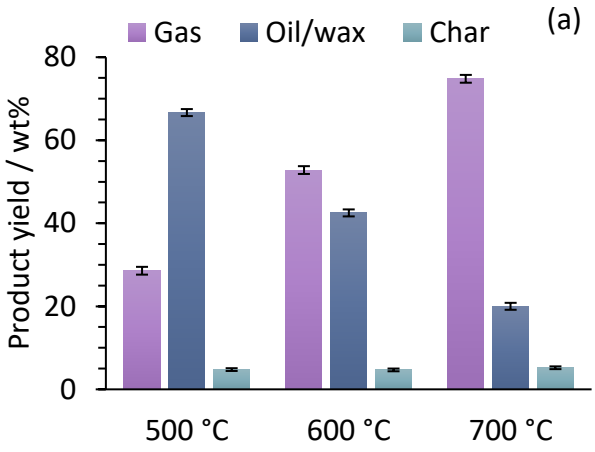

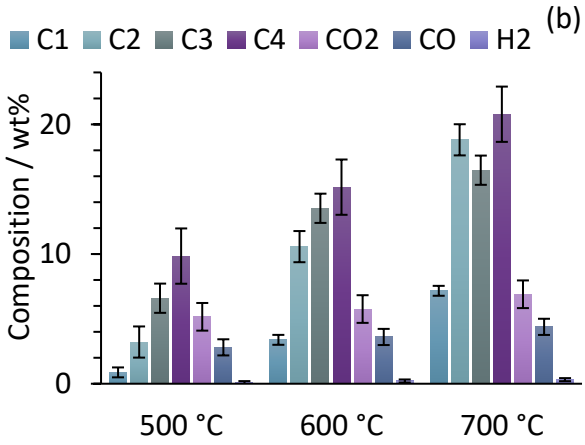

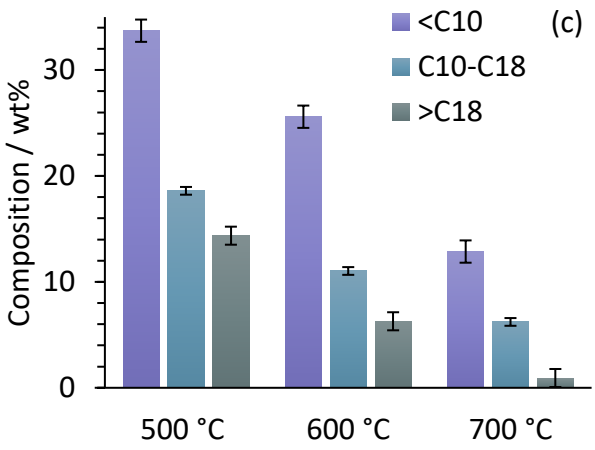

Figure 5. Product yields (a), gas composition (b), and oil composition (c) of non-catalytic pyrolysis at different catalyst bed temperatures.

Table 3. Summary of non-catalytic pyrolysis yields in literature and in this study.

Plastic mixture	Temperature / °C	Gas yield / wt%	Oil yield / wt%	Char / wt%	Reference
PP, PET, PS, LDPE, HDPE	500	31.7	66.6	1.7	[41]
	600	35.0	61.7	3.3	
	700	38.3	60.0	1.7	
	800	51.7	46.6	1.7	
PP, PET, PS, LDPE, HDPE	500	5	86	9	[42]
PP, PET, PS, HDPE, PVC	500	41.5	53	5.5	[43]
PP, PVC, HDPE, ABS, PS	500	15 - 25	70 – 80	10 – 15	[44]
PP, PET, PS, PE, PVC	500	34	65.2	0.8	[45]
PP, PET, PS, LDPE, HDPE, PVC	500	9.8	55.1	2.8	[46]
	550	24.5	57.1	5.9	
	600	43.3	43.2	7.6	
	650	88.8	20.5	--	
	700	68.9	18.4	--	
PP, PET, PS, LDPE, HDPE	500	28.6	66.7	4.8	This study
	600	53.2	42.5	4.3	
	700	74.8	20.0	5.2	

The gas composition (Figure 5(b)) primarily consisted of C_1 – C_4 hydrocarbons (71 – 84 wt% with respect to the total gas yields), along with minor quantities (16 – 29 wt%) of H_2, CO, and CO_2. The yields of CO and CO_2 increase at higher temperatures ($\geq$600 °C), which can be attributed to PET decarboxylation reactions within the mixed plastic waste [47]. Furthermore, at reaction temperatures $\geq$600 °C, CO_2 interacted with plastic volatiles through hydrocarbon dry reforming reactions to produce CO and H_2 ($xCO_2 + C_xH_y \rightarrow 2xCO + \frac{y}{2}H_2$) [48]. H_2 was detected across all experimental conditions, but production remained relatively low compared to other components, with a maximum yield of only 0.31 wt% at 700 °C. Elevated temperatures during pyrolysis of plastics facilitated the cleavage of C-C bonds at arbitrary positions along the polymer or hydrocarbon chain, with an average paraffinic bond energy of 83 kcal mol^{-1}, through a random chain scission mechanism [49]. Consequently, as the reaction proceeded, each remaining bond exhibited an equal likelihood of rupture, thereby generating a diverse range of hydrocarbons from C_1 to C_{30+} [41]. Concurrently, the cleavage of carbon-hydrogen (C-H) bonds was restricted, with an average paraffinic bond energy of 97 kcal/mol

[49], resulting in a minimal release of H_2. The yields of light gases (C_1-C_4) increased significantly with temperature. At 500 and 600 °C, the yield of C3 compounds was higher than those of C_1 and C_2. However, as the temperature rises to 700 °C, the rate of increase of propane and propylene was less pronounced compared to those of ethane and ethylene since there was a higher conversion of heavier compounds ($\geq C_3$) into lighter gaseous molecules (C_1 and C_2) at these conditions, as evidenced in Figure 5(b).

The liquid products (Figure 5(c)) consisted of a mixture of oil and wax, with their relative proportions varying based on the processing conditions (i.e., 4.6 – 21.5 wt% with respect to the total liquid products). Approximately 300 distinct compounds were identified, most of which were present in relatively low concentrations. The light hydrocarbon fraction, which corresponds to the carbon number range of naphtha [50], was predominant under all examined conditions during non-catalytic pyrolysis. A reduction in all fractions was observed with increasing temperature, which is attributable to the conversion of these compounds into gaseous hydrocarbons via thermal cracking reactions. The main change in the oil products with operating temperature was the marked decrease in the wax content, significantly decreased as the pyrolysis temperature increased. The mass percentage of wax with respect to the total oil yield was 21.5 wt% at 500 °C, which decreased to 14.5 wt% at 600 °C. With a subsequent increase to 700 °C, the wax fraction was further reduced to a negligible 4.6 wt%.

3.3. Catalytic pyrolysis

3.3.1. Raw AC

The Raw-AC exhibited moderate catalytic effects, with product yields displayed in Figure 6. Contrasting with non-catalytic pyrolysis, the Raw-AC catalysed process at 500 °C yielded a lower oil/wax output (60 wt% vs. 67 wt%) and a higher gas production (35 wt% vs. 29 wt%). Upon increasing the temperature to 600 °C, the differences between both processes became negligible. At 700 °C, the gas yield from Raw-AC catalysed pyrolysis surpassed that of the non-catalytic run, reaching 78 wt% compared to 75 wt%. These findings revealed that Raw-AC may exert a small catalytic influence on product yields at low and high temperatures.

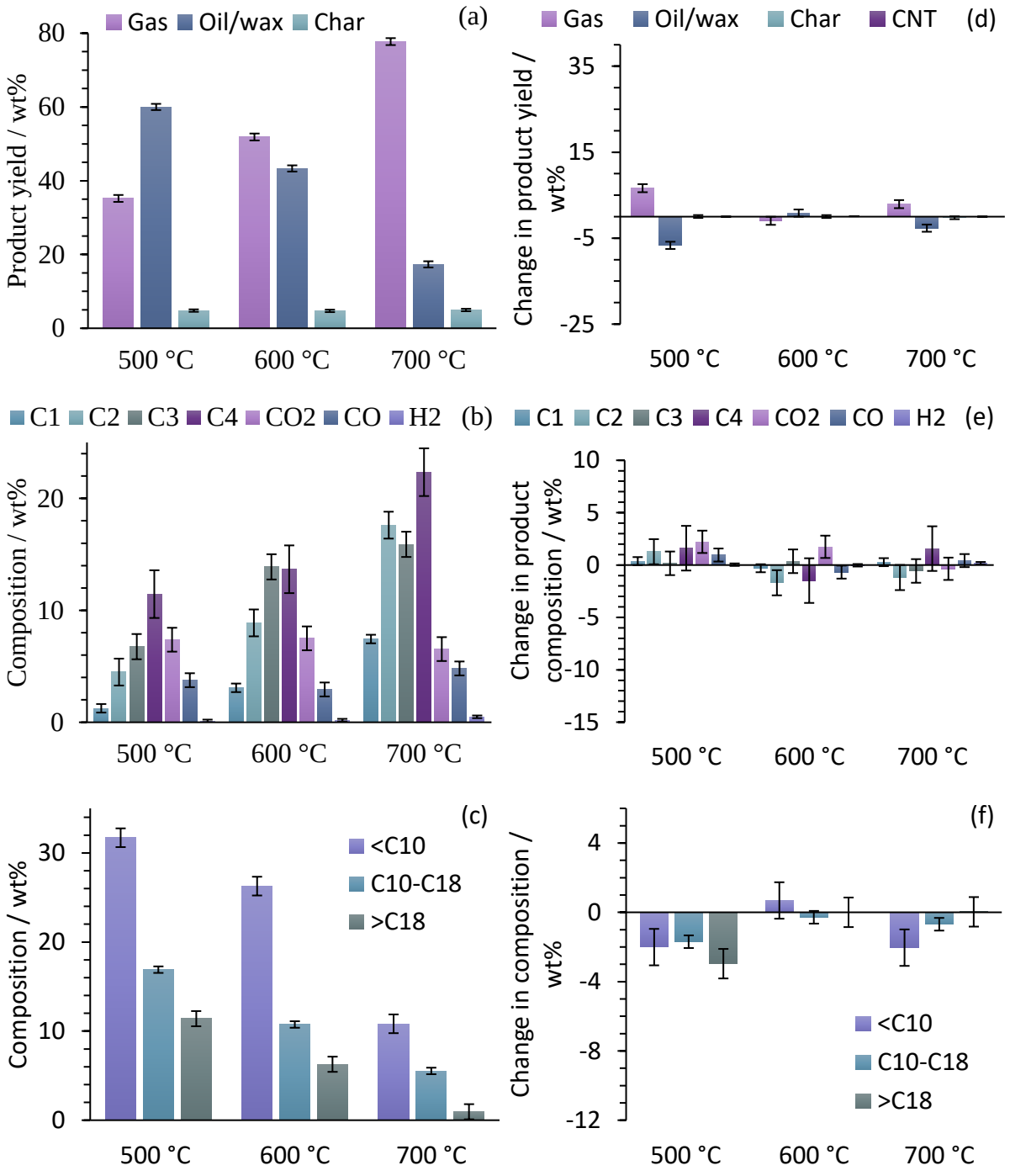

Figure 6. Product yields (a), gas composition (b), and oil composition (c) of pyrolysis-catalysis using Raw AC at different catalyst bed temperatures. (d) – (f) Analogous plots showing the wt% change in product yields and compositions versus the non-catalytic pyrolysis stage-only values presented in Figure 5.

The influence of Raw-AC on gas composition at 500 °C, as illustrated in Figure 5.8(a), was evident in the enhanced CO_2 production, yielding 7.38 wt% compared to 5.15 wt% in the non-catalysed process. This increase may stem from minor oxidation reactions facilitated by the

AC, as a similar marginal increment was observed across all AC-catalysed runs at low temperature (500 °C). At 600 °C, the gas composition results corresponded with the yield findings, with no substantial differences in product formation, except for CO_2, which rose from 5.76 wt% to 7.50 wt%.

Regarding oil/wax composition (Figure 5.8(b)), all results lied within the experimental error margins; thus, no significant differences in liquid product compositions were discernible between Raw-AC catalysed pyrolysis and non-catalytic pyrolysis across the investigated temperature range.

3.3.2. Nickel-incorporated AC

Reports of catalytic cracking of short chain alkanes in the literature suggest a possible sequence for the catalysis process: volatile hydrocarbons undergo dissociative chemisorption on the nickel surface, forming adsorbed reactive hydrocarbon fractions (e.g., methyl and methylene radicals) which can then participate in subsequent reactions [51]. The subsequent transformations involve the rearrangement of carbon atoms on the nickel particle surface and yields gaseous products (e.g., C_1-C_4, and H_2) and solid carbon.

The production of gaseous and oil/wax compounds (Figure 7(a)) demonstrated a similar pattern in response to increasing temperatures as the non-catalytic pyrolysis process. However, at 600 °C, the gas yield was lower than that obtained from the non-catalytic experiments (42 wt% compared to 53 wt%). The oil yield also decreased (with 30 wt% in contrast to 43 wt% during non-catalytic pyrolysis). This phenomenon can be attributed to the generation of carbon CNTs on the catalyst surface, as their formation occurs at the expense of gaseous and liquid byproducts. Figure 8 presents a comparison of the Ni-AC catalyst surface before and after pyrolysis at 600 °C, clearly showing the formation of CNTs as an entangled array of narrow “line like” features. The diameters of the CNTs were approximately 30 nm.

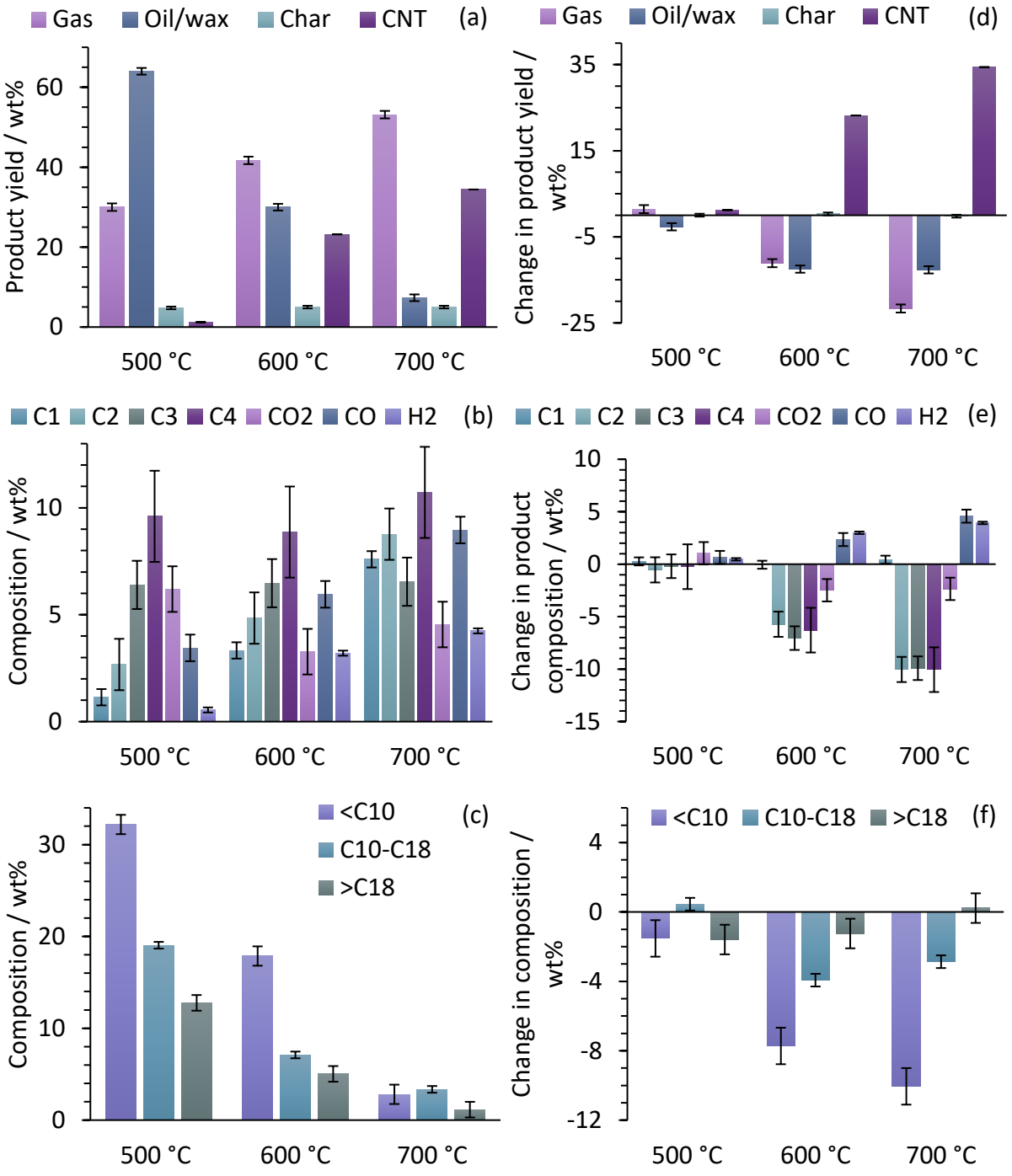

Figure 7. Product yields (a), gas composition (b), and oil composition (c) of pyrolysis-catalysis using Ni-AC at different catalyst bed temperatures. (d) – (f) Analogous plots showing the wt% change in product yields and compositions versus the non-catalytic pyrolysis stage-only values presented in Figure 5.

As illustrated in Figure 7(a), temperatures exceeding 600 °C promoted CNT formation. The nickel particles in the AC serve as catalysts for CNT growth by promoting the breakdown of hydrocarbon molecules and enabling the rearrangement of carbon atoms into a filamentous

nanotube configuration [52]. Nickel promotes the cleavage of C-H bonds [53] which can result in subsequent reactions such as functionalisation, rearrangement, or coupling reactions. The high formation of carbon nanotubes promoted by Ni-AC could be explained by the enhanced C-H cleavage which leads to coupling reactions in which new C-C bonds are formed and rearranged into CNTs. The CNT yield increased from a negligible 1.2 wt% to 23.2 wt% upon increasing the temperature from 500 to 600 °C and continued to rise to 34.4 wt% at 700 °C.

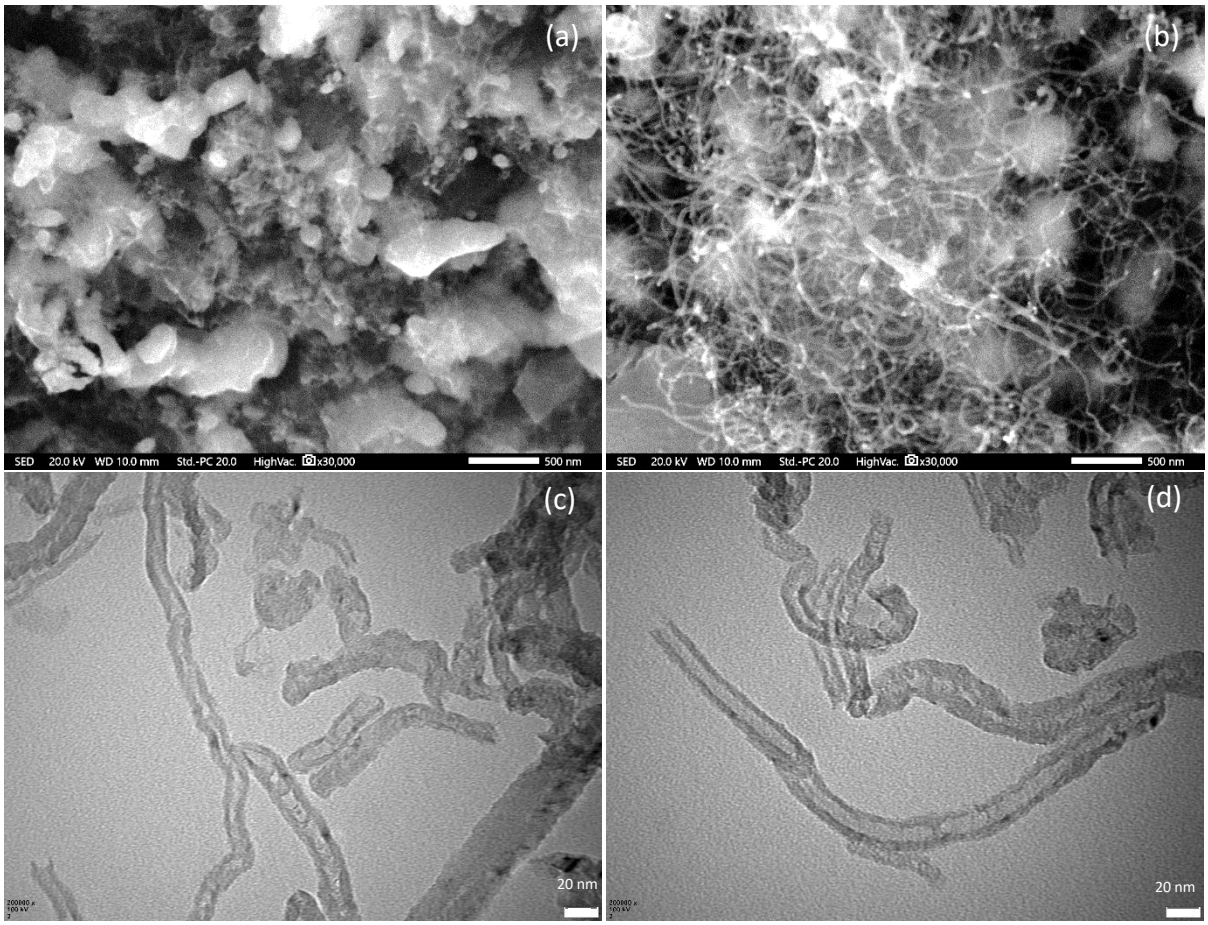

Figure 8. SEM comparison of fresh (a) and spent (b) Ni-AC, and TEM images (c-d) showing the morphology and size of the synthesized carbon nanotubes.

At 700 °C, CNT synthesis occurred at the expense of the liquid portion of the products as well as the gaseous fraction, as evidenced by the significantly reduced gas and oil production versus the Raw-AC, 53 and 7.3 wt% down from 78 and 20 wt%, respectively. This implies consumption of the thermal products produced in the first stage by the second catalytic stage to form CNTs.

The production of C_1 (Figure 7(b)) demonstrated a consistent positive correlation with temperature and showed a significant increase when the temperature is increased from 600

to 700 °C, resulting in the yield more than doubling from 3.3 wt% to 7.6 wt%. This also significantly exceeded the yield seen from the output of the non-catalytic pyrolysis or in the Raw-AC case, implying the change results from the Ni-AC catalysing a reaction. The yields of ethane and ethylene followed a comparable increasing trend with temperature, while maintaining consistent proportions relative to one another, but now with lower overall production than the non-catalytic benchmark. Conversely, the production of propane and propylene remained stable across the entire temperature range examined. These observations imply that the primary thermal cracking of long-chain hydrocarbons led to an enhanced generation of lighter molecules such as C_1, and C_2 compared to C_3. The production of C_1 and C_2 compounds may also be favoured due to secondary dehydrogenation reactions facilitated by the Ni-AC catalyst in conjunction with the temperature conditions. As a result, it can be inferred that the Ni-AC catalyst exhibited high selectivity for C1 and C2 compounds over C3. A similar conclusion can be drawn for C_4 compounds, which displayed a similar variability as C_3 compounds. The yield of CO_2 exhibited minor fluctuations within the range of 3.3 wt% to 6.2 wt%. Conversely, CO production demonstrated a consistent increase, nearly doubling for each 100 °C temperature increment. Specifically, CO yield increased from 3.5 wt% to 6 wt% as temperature rose from 500 to 600 °C, and further augmented to 9 wt% at 700 °C. This behaviour can be attributed to the catalytic influence of nickel particles, which promote Boudouard and hydrocarbon reforming reactions at elevated temperatures (>600 °C) [48]. The Boudouard reaction generates CO through the combination of carbon and CO_2, while the reforming reaction transforms CO_2 and hydrocarbons into CO and H_2. These mechanisms also adduce the enhanced production of H_2, which markedly increases from 0.5 wt% to 3.2 wt% upon increasing the temperature from 500 to 600 °C, and subsequently to 4.2 wt% at 700 °C. Although the H_2 yield may appear comparatively low, the volume percentage of H_2 in the gaseous product mixture at 600 and 700 °C constituted 62.1 and 57.7 vol%, respectively. It is important to note that these reactions are not prominent at 500 °C, meaning that temperatures of around 600 °C or higher are required to optimise H_2 and CO production. The mixture of these gases, referred to as syngas, is an important commercial product due to its role as a precursor for numerous industrial chemicals (e.g., alcohols, olefins, and ammonia) through advanced chemical manufacturing processes such as the Fischer-Tropsch synthesis [54].

As in the case of non-catalytic experiments, a consistent decrease in oil/wax yields was observed, maintaining relatively stable proportions among the three liquid hydrocarbon fractions, as illustrated in Figure 7(c). However, a significant reduction in the light fraction ($<C_{10}$) occurred at 700 °C. The relative proportion of the light fraction to the total oil yield exhibited a minor increase from 50.3% at 500 °C to 59.5% at 600 °C, followed by a drastic decline to 38.5% at 700 °C. This indicates that at elevated temperatures ($\geq$700 °C), the products favoured by the Ni-AC catalyst, such as CO, H_2, and CNTs, were predominantly generated at the expense of the light oil fraction.

3.3.3. Iron-incorporated AC

The product yields from catalytic pyrolysis using Fe-AC are presented in Figure 9. When comparing the outcomes of the non-catalytic runs to those employing Fe-AC, the oil/wax yields at 500 °C were slightly lower (60 wt% vs. 66.6 wt%), while the gas yield was higher by a similar magnitude (28.6 wt% vs. 35.1 wt%). However, at 600 °C, the oil/wax yields remained practically unchanged, but the gas yield declined to 45.7 wt% in the presence of Fe-AC compared to 52.8 wt% in non-catalytic runs. Under these conditions, the CNT yield experienced a substantial increase (from 0.1 wt% at 500 °C to 7.8 wt% at 600 °C), suggesting that CNT formation at 600 °C primarily occurred at the expense of gaseous compounds. This behaviour became more pronounced at 700 °C, with both liquid and gas yields decreasing by approximately 6 wt% compared to non-catalytic runs. The lower gas yields, particularly at elevated temperatures (600-700 °C), can be explained by the shift in product distribution towards CNTs, as more carbon is consumed from the plastic volatiles for the growth of CNTs instead of forming gaseous hydrocarbons. The yield of CNTs was negligible at 500 °C; however, as the temperature rose to 600 and 700 °C, the CNT formation increased to 7.8 wt% and 12.27 wt%, respectively. Figure 10 shows a comparison of the Fe-AC catalyst surface before and after pyrolysis, illustrating the formation of carbon nanotubes, which had a diameter of approximately 60 nm.

The high production of CO_2 at 500 °C (Figure 9(b)) may be ascribed to a minimal extent of carbon oxidation within the AC. This is corroborated by the slightly increased yields of CO_2 (1.7 wt% on average) observed in the AC-catalysed experiments compared to their non-catalytic counterparts. However, with rising temperatures and considering the restricted oxygen presence in the plastic sample, the formation of CO_2 gradually shifted toward CO. The

CO yield notably increased at higher temperatures, with 3 wt% at 500 °C, 6.1 wt% at 600 °C, and 10.8 wt% at 700 °C. This occurrence can be explained by the catalytic influence of iron particles, which facilitate hydrocarbon reforming reactions, yielding CO and H_2. Consequently, the H_2 production significantly increased at high temperatures (0.28 wt% at 500 °C, 1.32 wt% at 600 °C, and 1.97 wt% at 700 °C). The substantial H_2 release is directly correlated with the formation of CNTs, as the cleavage of C-H bonds is intensified, and a substantial supply of carbon atoms becomes accessible for CNT synthesis.

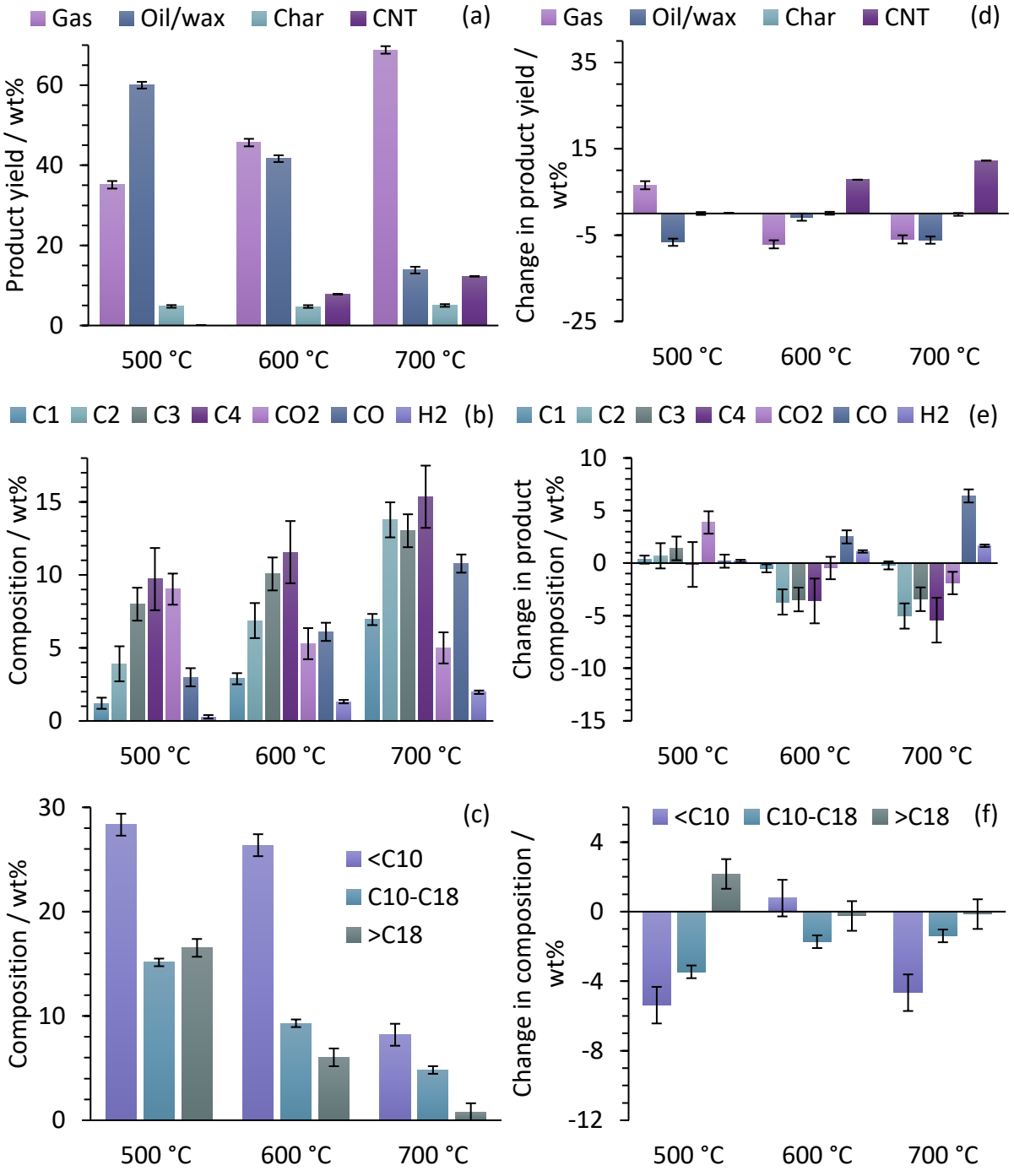

Figure 9. Product yields (a), gas composition (b), and oil composition (c) of pyrolysis-catalysis using Fe-AC at different catalyst bed temperatures. (d) – (f) Analogous plots showing the wt% change in product yields and compositions versus the non-catalytic pyrolysis stage-only values presented in Figure 5.

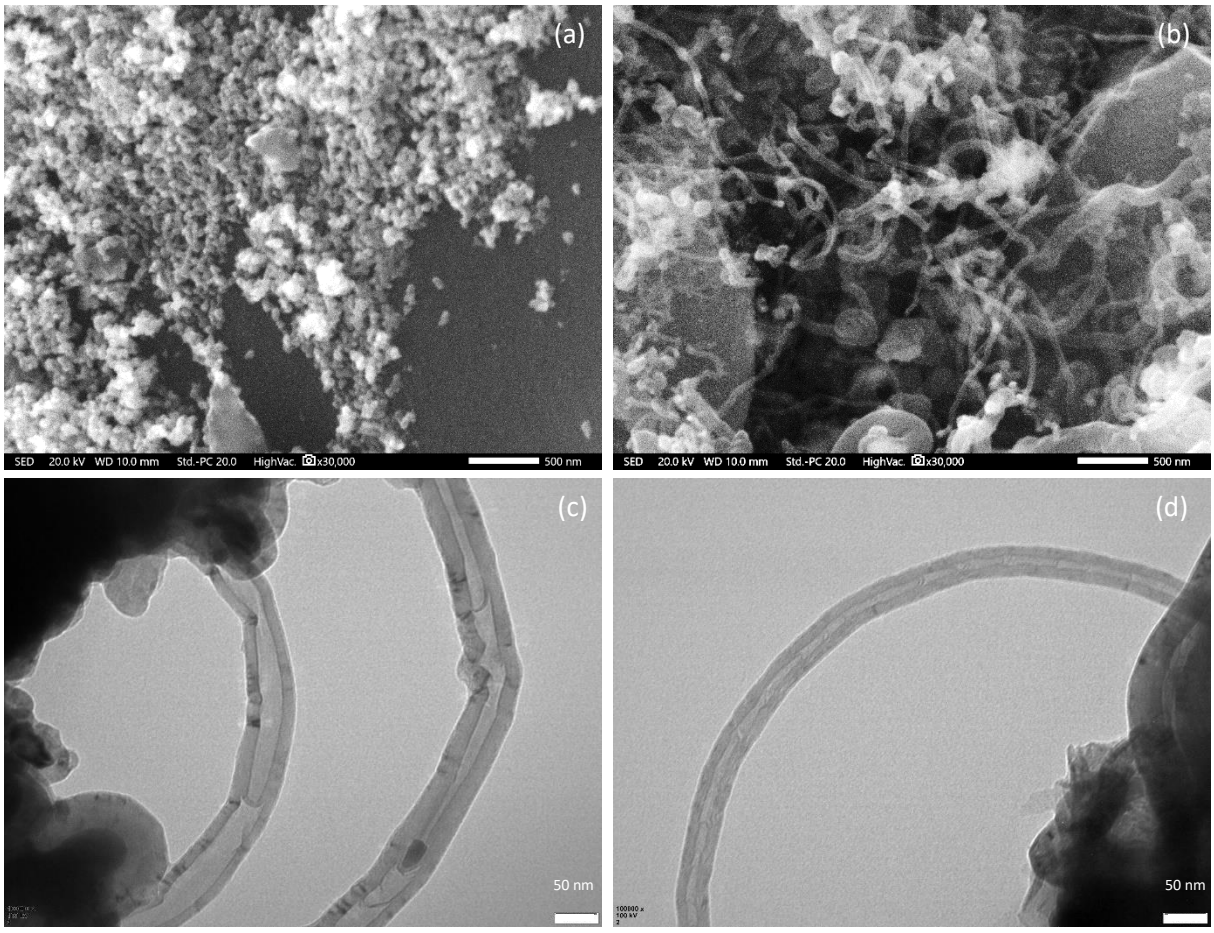

Figure 10. SEM comparison of fresh (a) and spent (b) Fe-AC, and TEM images (c-d) showing the morphology and size of the synthesized carbon nanotubes.

The yields of C_1-C_4 gases (Figure 9(b)) exhibited a similar increase with temperature, as observed in prior experiments. As the temperature increased from 500 to 600 °C, their relative rates of increase were analogous, but ethane and ethylene production at 700 °C surpassed that of other hydrocarbon gases. This implies that the catalytic cracking of high molecular weight hydrocarbons in the presence of Fe-AC at 700 °C was intensified, and the catalyst exhibited heightened selectivity toward C_2 compounds, of which the majority (73% of C_2 compounds) was ethylene. The formation of light paraffins and olefins is favoured due to the additional hydrogenation reactions and C-H bond cleavage facilitated by the catalyst.

512 The high yield of the light oil fraction at 600 °C (Figure 9(c)) supports previous assertions that
513 CNT formation predominantly arises from the gaseous products. Conversely, at 700 °C, a
514 substantial decline in the light oil fraction was detected, indicating a higher catalytic
515 selectivity for H_2, CO, light hydrocarbon gases, and CNT formation over light oil products.

516 *3.3.4. Zinc-incorporated AC*

517 The product yields from Zn-AC catalysed pyrolysis (Figure 11(a)) were similar to those
518 obtained from non-catalytic pyrolysis. At a temperature of 500 °C, the oil/wax yield reached
519 63 wt%, while the yield for non-catalytic pyrolysis was marginally higher at 67 wt%.
520 Concurrently, the gas yield was 31.9 wt%, compared to a slightly lower yield of 29 wt% for the
521 non-catalytic pyrolysis. At 600 °C, the discrepancies in product yields between both processes
522 became insignificant. At 700 °C, the Zn-AC catalysed pyrolysis produced an oil/wax yield of 23
523 wt%, which is 17 % higher than the non-catalytic counterpart. The corresponding Zn-AC gas
524 yield, however, was 72 wt%, constituting a 4 % decrease compared to the non-catalytic runs.
525 Overall, the Zn-AC catalyst exhibited a subtle inclination towards gas yield at 500 °C, an
526 inconsequential effect at 600 °C, and a slight preference for oil/wax formation over gaseous
527 products at 700 °C. Nonetheless, the distinctions between the catalytic and non-catalytic
528 processes remained relatively mild, and the catalytic activity of Zn particles on AC was
529 significantly lower than that of Ni-AC and Fe-AC. Carbon deposition on the catalyst surface
530 was found to be negligible (0.3 – 0.7 wt%), therefore, these results were omitted from Figure
531 11(a).

532 The compositions of gas and oil/wax products are illustrated in Figure 11(b). The most notable
533 variation in gas compositions lied in the CO_2 yield at lower temperatures (<700 °C), where the
534 presence of the Zn-AC catalyst led to an increase compared to the non-catalytic pyrolysis runs.
535 At 500 °C, the CO_2 production for the catalytic process was 6.6 wt%, whereas the non-catalytic
536 process produced 5.1 wt%. This difference persisted at 600 °C, with the catalysed CO_2 yield at
537 7.6 wt% and the non-catalytic yield at 5.7 wt%. However, the CO_2 yields for both processes
538 converged at 700 °C. The remaining gas components exhibited negligible differences at
539 corresponding temperatures in comparison to the non-catalytic pyrolysis, as they fell within
540 the respective experimental error margins.

541

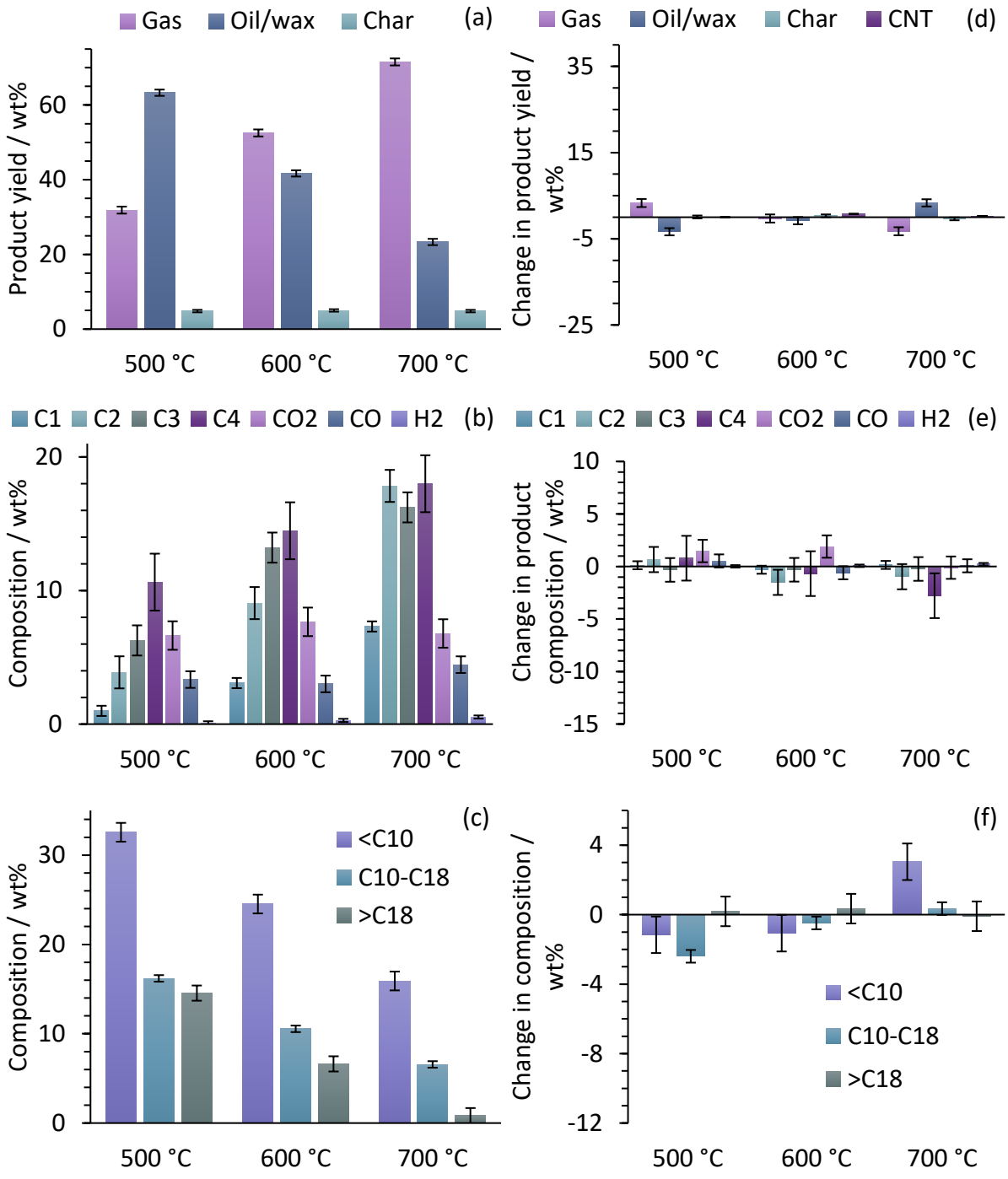

Figure 11. Product yields (a), gas composition (b), and oil composition (c) of pyrolysis-catalysis using Zn-AC at different catalyst bed temperatures. (d) – (f) Analogous plots showing the wt% change in product yields and compositions versus the non-catalytic pyrolysis stage-only values presented in Figure 5.

As shown in Figure 11(c), the most pronounced difference in the oil/wax composition at 500 °C involves the medium oil fraction, which was marginally lower in the Zn-AC catalysed process compared to the non-catalytic process (16.2 wt% vs. 18.6 wt%). This indicated that

552 the reduction in the medium oil fraction primarily contributed to the overall decrease in liquid
553 product yield observed in Figure 11(a), as some of this fraction was converted into gaseous
554 products, consequently resulting in a modest increase of the gas yield. At 600 °C, no
555 statistically significant disparities in oil/wax composition were detected between the
556 catalysed and uncatalyzed experiments, which is consistent with the negligible differences
557 observed in product yields at this temperature. However, upon increasing the temperature
558 to 700 °C, the light oil fraction exhibits a higher value (15.9 wt% vs. 12.86 wt%), accounting
559 for the higher oil/wax yield and lower gas yield at this elevated temperature.

560 *3.3.5. Zeolite H-ZSM-5*

561 Zeolite H-ZSM-5 demonstrated a significant impact on the product yield distribution,
562 favouring the production of lighter gaseous compounds, as shown in Figure 12. When
563 comparing the catalytic process to non-catalytic pyrolysis at 500 °C, the H-ZSM-5 zeolite
564 promoted a notable decrease in the oil/wax yield from 66.6 wt% to 46.7 wt%, alongside a
565 concurrent increase in the gas yield from 29 wt% to 48 wt%. The observed outcomes
566 demonstrate the effectiveness of the H-ZSM-5 zeolite in cleaving long-chain hydrocarbons
567 present in plastic waste volatiles into lighter gaseous compounds at moderately low
568 temperatures. This behaviour can be attributed to the distinct physicochemical characteristics
569 of the H-ZSM-5 zeolite, which exhibits pronounced acidity and high shape selectivity [55]. The
570 acidic sites of the zeolite facilitate the scission of C-C bonds within long-chain hydrocarbon
571 molecules, whereas its well-organized pore structure promotes diffusion and enables the
572 selective conversion of specific hydrocarbons [56, 57]. At 600 °C, the differences between the
573 catalysed and non-catalysed processes became slightly less evident, but the influence of H-
574 ZSM-5 zeolite on product yields remained discernible. The oil/wax yield reduced from 43 wt%
575 to 37 wt%, while the corresponding gas yield exhibited an increase from 53 wt% to 58 wt%.
576 Upon further increasing the temperature to 700 °C, H-ZSM-5 catalysis lead to an additional
577 decrease in oil/wax yield to 16.6 wt%, and an increase in gas yield to 78 wt%. These findings
578 demonstrate that the H-ZSM-5 catalyst exerts a substantial impact on the distribution of
579 product yields.

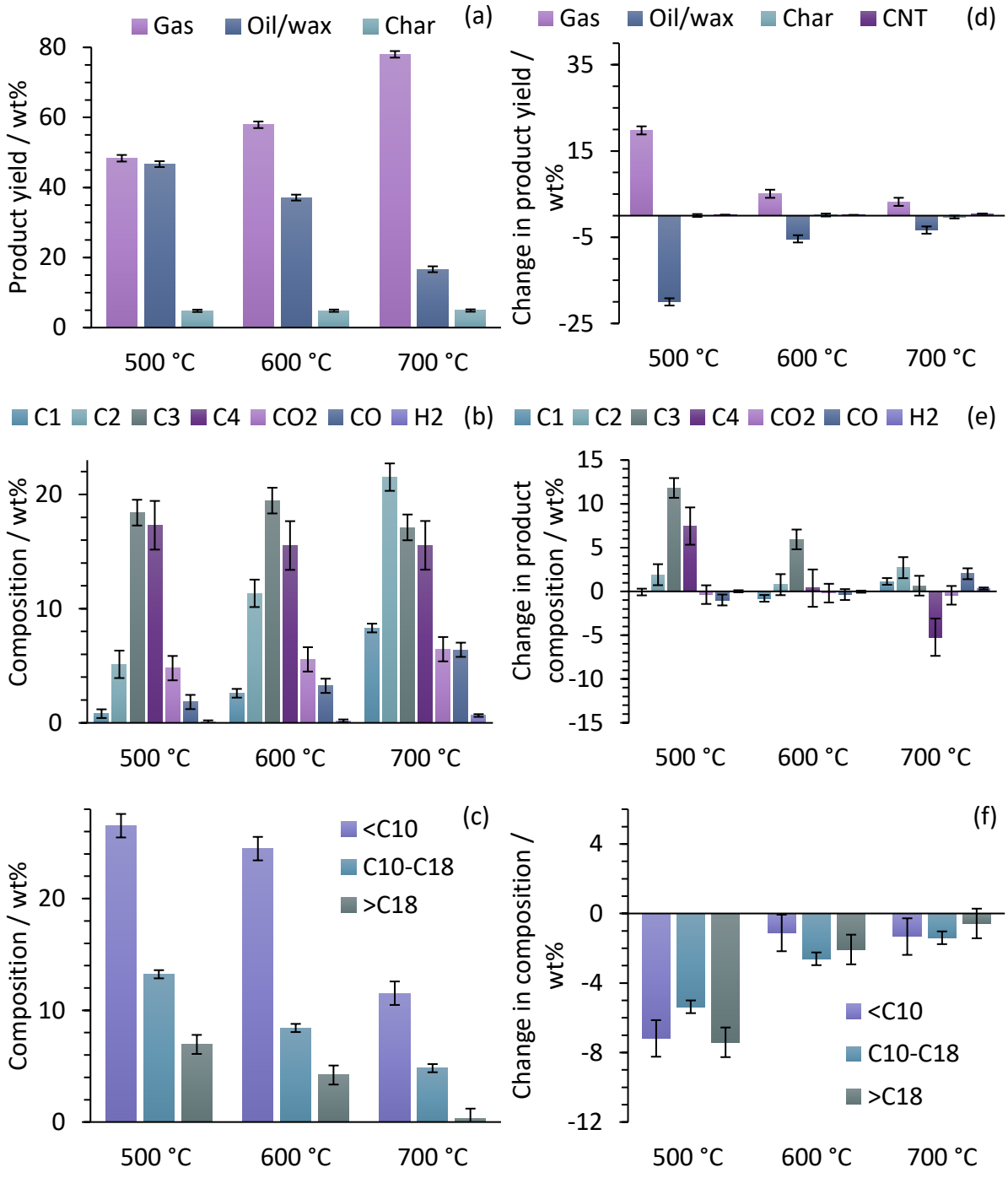

Figure 12. Product yields (a), gas composition (b), and oil composition (c) of pyrolysis-catalysis using zeolite H-ZSM-5 at different catalyst bed temperatures. (d) – (f) Analogous plots showing the wt% change in product yields and compositions versus the non-catalytic pyrolysis stage-only values presented in Figure 5.

The carbon accumulation on the catalyst was minimal (<0.5 wt%), demonstrating the efficacy of the two-stage reactor design in averting catalyst deactivation due to excessive carbon deposition, which can result in pore obstruction.

590 Although the differences in liquid and gaseous product yields (catalytic vs. non-catalytic
591 pyrolysis) were less pronounced at high temperatures (>600 °C), with differences of
592 approximately ± 5 wt%, the product quality was significantly enhanced, favouring lighter
593 compounds over heavier ones. The gas product composition depicted in Figure 12(b) shows
594 that at 500 °C, H-ZSM-5 zeolite significantly enhanced C_3 compounds yield from 6.6 wt% to
595 18.4 wt% (of which 78.3% is propylene). Furthermore, C_4 gas production notably increased
596 from 9.8 wt% to 18.4 wt%, ethane and ethylene production slightly rose from 3.2 wt% to 5.1
597 wt%, and CO yield moderately decreased from 2.8 wt% to 1.8 wt%. The primary product
598 resulting from the conversion of volatiles into gases at low temperature was predominantly
599 propylene, a valuable monomer in the chemical manufacturing industry. As the temperature
600 increased to 600 °C, the only significant difference was observed in the C_3 compounds, with
601 propane and propylene production increasing from 13.5 wt% to 19.5 wt% (of which 91.2% is
602 propylene), and the remaining products staying within the experimental error. This
603 observation corresponds with the approximately 5.5 wt% gas yield increase at this
604 temperature, indicating that H-ZSM-5 zeolite selectively converted liquid products into
605 propane and propylene. These outcomes are consistent with findings reported in the
606 literature, where high conversion of plastic waste volatiles into propylene has been achieved
607 using zeolite H-ZSM-5 catalyst [58-60]. At 700 °C, H_2 production doubles to 0.64 wt%, CO and
608 C_1 yields moderately rise from 4.4 wt% to 6.4 wt% and from 7.1 wt% to 8.3 wt%, respectively.
609 Owing to enhanced thermal cracking, C_4 compound production declined from 21 wt% to 16
610 wt%, while C_2 compounds yield increased from 19 wt% to 22 wt%.

611 The liquid product composition was significantly influenced by the H-ZSM-5 catalyst, as
612 illustrated in Figure 12(c). All oil/wax fraction yields at 500 °C were lower than those observed
613 in non-catalytic pyrolysis. At 500 °C, the light fraction increased from 50.6 wt% to 56.8 wt%
614 (with respect to the total liquid product yield) in the presence of H-ZSM-5 zeolite, while the
615 medium fraction remained relatively constant (around 28%), and the heavy wax decreased
616 from 21.5% to 14.9%. At 600 °C, no significant differences were observed in light oil yields,
617 which were approximately 25 wt%. At 700 °C, the relative amount of light fraction with
618 respect to the total oil yield increased from 64.3 wt% to 69.1 wt%, while the medium fraction
619 and heavy wax decreased from 31.1% to 28.9%, and 4.6% to 2.1%, respectively. The H-ZSM-5
620 catalysed pyrolysis yielded a higher proportion of light oil and a lower proportion of heavy

wax at all three temperatures compared to non-catalytic pyrolysis. The gas and liquid product compositions support the notion that H-ZSM-5 zeolite enhances the production of light molecules at the expense of heavier ones. This is achieved through a series of complex reactions, including cracking, cyclization, and isomerization, occurring at the zeolite's active sites [61]. As a result, the overall yield of heavy wax is substantially reduced, demonstrating the effectiveness of H-ZSM-5 zeolite in cracking long-chain hydrocarbons, particularly at relatively low temperatures during plastic waste pyrolysis.

3.3.6. Catalyst performance comparison

A higher catalytic activity was observed for Ni-AC, Fe-AC, and H-ZSM-5 in comparison to Zn-AC and Raw AC. The influences of Ni-AC and Fe-AC catalysts on the process displayed analogous patterns, with the production of H_2, CO, and CNTs (exclusively identified with Ni-AC and Fe-AC) rising as the temperature increases. Regarding product yields, the process was similar for both catalysts at 500 °C; however, as the temperature increases, the yields of gaseous and liquid products catalysed by Ni-AC progressively decreased, concomitant with an increase in CNT production. An intensified formation of CNTs was attained using the Ni-AC catalyst compared to those obtained with Fe-AC (1.2 wt% vs. 0.1 wt% at 500 °C, 23.2 wt% vs. 7.8 wt% at 600 °C, and 34.4 wt% vs. 12.3 wt%). Consequently, it can be inferred that Ni-AC is more effective at producing high yields of CNTs (and the associated increase in H_2 yields). This finding contrasts with other studies in the literature. For instance, Liu et al. [62] compared the effects of iron, nickel, and cobalt on metal oxide supports as catalysts for CNT synthesis from methane at 900 °C, concluding that iron produces higher quality CNTs. This was attributed to iron's high carbon solubility, which impacts CNT nucleation and growth through various mechanisms, such as: (i) enhancing carbon supply for CNT development; (ii) generating a higher concentration force to expedite CNT formation; (iii) influencing CNT cap structure nucleation; and (iv) dictating the specific CNT variety produced [62, 63]. Acomb et al. [31] compared the effects of several metal oxides including iron alumina and nickel alumina on CNT formation from plastic waste at 800 °C, and also found iron to be more effective (i.e., higher yields) than nickel. The higher carbon solubility of iron compared to that of nickel was determined to be responsible for the higher CNT yields. Moreover, the interactions between the metal and the catalyst support were found to play a crucial role in CNT formation, with excessively strong interactions inhibiting production and weak interactions leading to metal

652 sintering and low yields [31]. Since iron has a higher carbon solubility than nickel, there may
653 be a stronger interaction between the AC support and iron particles, thus hindering CNT
654 formation. Nonetheless, this interaction is not excessively strong, as Fe-AC still allowed some
655 CNT formation, albeit in lower amounts than those obtained using Ni-AC. It can be concluded
656 that nickel and iron particles exhibit an intermediate interaction with the AC, enabling carbon
657 nanotube formation. These results demonstrate that AC is a suitable support for nickel and
658 iron catalysts in facilitating plastic waste pyrolysis.

659 The surface areas and pore volumes of spent Ni-AC and Fe-AC catalysts are shown in Table 4.
660 The mesopore volume (V_{meso}) of Ni-AC increased significantly from 0.024 to 0.156 $cm^3\ g^{-1}$,
661 while the micropore volume ($V_{DR\ N2}$) was reduced from 0.123 to 0.055 $cm^3\ g^{-1}$. This resulted
662 in a total pore volume increase of 42.8% (from 0.147 to 0.210 $cm^3\ g^{-1}$). After reaction, the
663 isotherm (Fig. S2) changes from Type I into Type II/IV isotherms, suggesting that the gas reacts
664 with carbon in Ni-AC catalyst and widens the pores, creating more mesopores at an expense
665 to micropores. Compared to the fresh catalyst, the BET surface area (S_{BET}) of Ni-AC decreased
666 from 308.36 to 129.23 $m^2\ g^{-1}$ after pyrolysis. This is explained by the formation of CNTs, which
667 can block pores and reduce the accessible surface area on the catalysts.

668 The gas-solid reactions with Fe-AC significantly consume the carbon in the catalyst and
669 decrease the S_{BET} (from 314.24 to 59.22 $m^2\ g^{-1}$), V_{total} (from 0.171 to 0.083 $cm^3\ g^{-1}$), and $V_{DR\ N2}$
670 (from 0.127 to 0.027 $cm^3\ g^{-1}$). The isotherm (Fig. S3) changes from type I/II into type II
671 isotherm after pyrolysis, which also indicates the reaction between carbon and gas. The
672 evident changes in pore volumes for both catalysts are a consequence of the restructuring of
673 the catalyst carbon matrix during CNT growth. The more pronounced structural changes in
674 Ni-AC compared to Fe-AC suggest that Ni is a more active catalyst for CNT growth in activated
675 carbon supports.

676 Table 4. Surface area and pore volume of catalysts after pyrolysis at 700 °C.

Catalyst	S_{BET} / $m^2\ g^{-1}$	V_{total} / $cm^3\ g^{-1}$	$V_{DR\ N2}$ / $cm^3\ g^{-1}$	V_{meso} / $cm^3\ g^{-1}$
Ni-AC spent	129.23	0.210	0.055	0.156
Fe-AC spent	59.22	0.083	0.027	0.056

677 Utilizing Zn-AC and Raw-AC catalysts resulted in a marginal decrease in liquid product yields
678 and a slight increase in gas yields compared to non-catalytic pyrolysis. However, these

679 catalysts exhibited limited efficacy since the product yields were similar to non-catalytic
680 pyrolysis when considering the experimental error range. Raw-AC displayed a slightly higher
681 catalytic performance compared to Zn-AC, with moderately increased gas yields and reduced
682 oil/wax yields. At 700 °C, the most significant difference was noted, as Raw-AC achieved a gas
683 yield of 77.7 wt% while Zn-AC only reached 71.5 wt%. This discrepancy can be attributed to
684 the substantial reduction in surface area (from 551.4 to 394.7 $m^2 g^{-1}$) and porosity (from 0.206
685 to 0.147 $cm^3 g^{-1}$) of Zn-AC after the wet impregnation method, whereas Raw-AC retains its
686 highly porous structure, providing access to internal active sites. Moreover, research has
687 suggested that temperatures exceeding 700 °C are necessary to sufficiently activate biochar
688 for pyrolysis or gasification processes [64-66]. Consequently, it can be inferred that Zn-AC was
689 not entirely activated at the temperatures examined in this study. Although the active sites
690 in Raw-AC exhibit much lower catalytic activity than those in Ni-AC and Fe-AC, the naturally
691 occurring metals present in the raw biochar become increasingly active as the temperature
692 intensifies, particularly at $\geq$800 °C [41].

693 The H-ZSM-5 catalyst displayed the most remarkable reduction in oil/wax yields and increase
694 in gas yields among all the catalysts examined, with these variations being significant across
695 all temperature ranges. Regarding oil/wax composition, H-ZSM-5 outperformed other
696 catalysts in converting heavy fractions to lighter counterparts. Moreover, H-ZSM-5 was the
697 most appropriate catalyst for monomer recovery, with ethylene and propylene yields
698 considerably higher than those observed with other catalysts (18 wt% and 16 wt% at 700 °C,
699 respectively). Ni-AC and Fe-AC also exhibited promising results, but with a markedly different
700 selectivity, with catalytic activities comparable to that of H-ZSM-5 but with selectivities
701 toward H_2, CO, and CNT production. Although all catalysts showed improved cracking at
702 elevated temperatures, H-ZSM-5 proved most effective at low temperature (500 °C).

703 For economic feasibility analysis and comparisons of the different catalysts' application,
704 various factors such as capital investments, maintenance costs, and scalability need to be
705 considered. However, these were all beyond the scope of this work, therefore, simple
706 comparisons on economic benefits can be based on the estimated values of key products.
707 According to 2024 forecasts, naphtha-range hydrocarbons are priced at approximately 0.64
708 USD kg^{-1} [67, 68], while short multi-walled CNTs (> 92% purity) cost around 487 USD kg^{-1} [69].
709 On a basis of 1 kg of plastic feed, the pyrolysis process for different catalysts would produce

710 the key product value presented in Table 5. For Raw-AC and Zn-AC, the main product was light
711 oil (produced at 500 °C), whereas for Ni-AC and Fe-AC, the key product were CNTs (produced
712 at 700 °C), assuming 100% generation efficiency.

713 Table 5. Comparison of key product value from different catalysts.

Catalyst	Light oil yield / kg	CNT yield / kg	Total key product value / USD $kg^{-1}_{plastic}$
Raw-AC	0.3171	--	0.203
Zn-AC	0.3255	--	0.208
Ni-AC	--	0.344	167.5
Fe-AC	--	0.123	59.9

714 The significant price disparity between light oil and CNTs likely stems from the high costs of
715 CNT production, extraction, purification, and classification, not accounted for in this study.
716 Moreover, the assumed 100% CNT generation efficiency is not guaranteed due to potential
717 amorphous carbon deposits on the catalysts. The results in Table 5 are intended for
718 comparative purposes only and do not reflect the actual revenue of an industrial-scale plant.
719 Such an assessment requires a dedicated technical and economic analysis, representing a
720 potential area for future research. Additionally, the study's products, particularly CNTs, need
721 further separation and processing before marketing, highlighting the need for additional
722 research into the separation and quality assessment of CNTs derived from plastic waste
723 pyrolysis.

724 ## 4. Conclusions

725 In this study, a comprehensive analysis of the performance of various catalysts, including Ni-
726 AC, Fe-AC, Zn-AC, Raw AC, and H-ZSM-5, for the pyrolysis of plastic waste was conducted. The
727 investigation primarily focused on the product yield distribution, composition, and carbon
728 nanotube formation. The key findings are outlined below:

729 - The Ni-AC and Fe-AC catalysts demonstrated superior catalytic activity compared to
730 Zn-AC and Raw AC. Both Ni-AC and Fe-AC displayed similar trends with increasing
731 temperature, resulting in enhanced yields of H_2, CO, and CNTs.
732 - The Ni-AC catalyst was more efficient in producing CNTs, yielding significantly higher
733 amounts than those obtained using Fe-AC.

- The CNTs synthesized using Ni-AC and Fe-AC possessed diameters of approximately 30 nm and 60 nm, respectively. The results demonstrated that AC is an appropriate support for nickel and iron catalysts, facilitating plastic waste pyrolysis.
- The Zn-AC and Raw-AC catalysts presented limited effectiveness compared to the other catalysts. Raw-AC outperformed Zn-AC, with moderately enhanced gas yields and reduced oil/wax yields.
- The H-ZSM-5 catalyst presented the most significant reduction in oil/wax yields and increase in gas yields across all examined temperature ranges. It surpassed other catalysts in converting heavy fractions into lighter counterparts and proved to be the most suitable catalyst for monomer recovery, with markedly higher ethylene and propylene yields. In contrast to the AC catalysts, syngas and CNTs are not produced.

Acknowledgements

This research was funded by the Mexican National Council of Humanities, Sciences, and Technologies (CONAHCYT) via PhD studentship 2019–000021–01EXTF-00104. SEM, EDX, GC-MS, and XRD analyses were provided by the Advanced Chemical and Materials Analysis (ACMA) unit at Newcastle University. HHP was supported by the Royal Academy of Engineering (Grant No: FF\1920\1\45), and The Royal Society (under Grant No: ICA\R1\191220) United Kingdom.

References

1. Roy, P., et al., *Microplastics in ecosystems: their implications and mitigation pathways.* Environmental Science: Advances, 2022. **1**(1): p. 9-29.
2. Edmond, C. *We know plastic pollution is bad–but how exactly is it linked to climate change*. in *World Economic Forum: https://www. weforum. org/agenda/2022/01/plastic-pollution-climate-change-solution/(Erişim Tarihi: 31.01. 2022)*. 2022.
3. PlasticsEurope. *Plastics–the Facts 2020*. 2020 [cited 2021 March]; Available from: https://www.plasticseurope.org/en/resources/publications/4312-plastics-facts-2020.
4. Nguyen, H.M. and M.L. Carreon, *Non-thermal Plasma-Assisted Deconstruction of High-Density Polyethylene to Hydrogen and Light Hydrocarbons over Hollow ZSM-5 Microspheres.* ACS Sustainable Chemistry & Engineering, 2022. **10**(29): p. 9480-9491.
5. Yao, L., et al., *Non-thermal plasma-assisted rapid hydrogenolysis of polystyrene to high yield ethylene.* Nature Communications, 2022. **13**(1): p. 885.
6. Shen, X., et al., *Microwave-assisted pyrolysis of plastics with iron-based catalysts for hydrogen and carbon nanotubes production.* Materials Today Chemistry, 2022. **26**: p. 101166.

7. Zhou, N., et al., *Catalytic pyrolysis of plastic wastes in a continuous microwave assisted pyrolysis system for fuel production.* Chemical Engineering Journal, 2021. **418**: p. 129412.

8. Mumtaz, H., et al., *Hydrothermal treatment of plastic waste within a circular economy perspective.* Sustainable Chemistry and Pharmacy, 2023. **32**: p. 100991.

9. Mukundan, S., et al., *hydrothermal co-liquefaction of biomass and plastic wastes into biofuel: Study on catalyst property, product distribution and synergistic effects.* Fuel Processing Technology, 2022. **238**: p. 107523.

10. Yang, R., et al., *Selective, Sequential, and "One-Pot" Depolymerization Strategies for Chemical Recycling of Commercial Plastics and Mixed Plastics.* ACS Sustainable Chemistry & Engineering, 2022. **10**(30): p. 9860-9871.

11. Qi, X., et al., *Evaluation of PET degradation using artificial microbial consortia.* Frontiers in Microbiology, 2021. **12**: p. 778828.

12. Satav, A.G., et al., *A state-of-the-art review on robotics in waste sorting: scope and challenges.* International Journal on Interactive Design and Manufacturing (IJIDeM), 2023.

13. Lubongo, C. and P. Alexandridis *Assessment of Performance and Challenges in Use of Commercial Automated Sorting Technology for Plastic Waste*. Recycling, 2022. **7**, DOI: 10.3390/recycling7020011.

14. Xu, D., et al., *Catalytic conversion of plastic wastes using cost-effective bauxite residue as catalyst into H-2-rich syngas and magnetic nanocomposites for chrome (VI) detoxification.* Journal of Hazardous Materials, 2021. **413**.

15. Adrados, A., et al., *Pyrolysis of plastic packaging waste: A comparison of plastic residuals from material recovery facilities with simulated plastic waste.* Waste Management, 2012. **32**(5): p. 826-832.

16. Xu, R., et al., *Development of metal-doping mesoporous biochar catalyst for co-valorizing biomass and plastic waste into valuable hydrocarbons, syngas, and carbons.* Fuel Processing Technology, 2022. **227**: p. 107127.

17. Bennett, J.A., et al., *Catalytic applications of waste derived materials.* Journal of materials chemistry A, 2016. **4**(10): p. 3617-3637.

18. Lin, X., et al., *The effects of pore structures and functional groups on the catalytic performance of activated carbon catalysts for the co-pyrolysis of biomass and plastic into aromatics and hydrogen-rich syngas.* Renewable Energy, 2023. **202**: p. 855-864.

19. Dong, Y., et al., *Effect of the catalyst pore structure on fixed-bed reactor performance of partial oxidation of n-butane: A simulation study.* Chemical Engineering Science, 2016. **142**: p. 299-309.

20. Escola, J.M., et al., *Catalytic hydroreforming of the polyethylene thermal cracking oil over Ni supported hierarchical zeolites and mesostructured aluminosilicates.* Appl. Catal., B, 2011. **106**(3): p. 405-415.

21. Serrano, D.P., et al., *Developing Advanced Catalysts for the Conversion of Polyolefinic Waste Plastics into Fuels and Chemicals.* ACS Catalysis, 2012. **2**(9): p. 1924-1941.

22. Serrano, D.P., et al., *Hierarchical Zeolites with Enhanced Textural and Catalytic Properties Synthesized from Organofunctionalized Seeds.* Chemistry of Materials, 2006. **18**(10): p. 2462-2464.

23. Zhang, X., et al., *The Role of External Acidity of Hierarchical ZSM-5 Zeolites in n-Heptane Catalytic Cracking.* ChemCatChem, 2018. **10**(12): p. 2655-2663.

24. van Deelen, T.W., et al., *Control of metal-support interactions in heterogeneous catalysts to enhance activity and selectivity.* Nature Catalysis, 2019. **2**(11): p. 955-970.

25. Johar, P., et al., *Biologically bound nickel accelerated de-polymerization of polyethylene to high value hydrocarbons and hydrogen.* RSC Sustainability, 2023.

26. Wang, C., et al., *Catalytic upcycling of waste plastics over nanocellulose derived biochar catalyst for the coupling harvest of hydrogen and liquid fuels.* Science of The Total Environment, 2021. **779**: p. 146463.

27. Wang, C.X., et al., *Application of highly stable biochar catalysts for efficient pyrolysis of plastics: a readily accessible potential solution to a global waste crisis.* Sustainable Energy & Fuels, 2020. **4**(9): p. 4614-4624.

28. Park, S., et al., *Continuous pyrolysis of organosolv lignin and application of biochar on gasification of high density polyethylene.* Applied Energy, 2019. **255**: p. 113801.

29. Nessim, G.D., *Properties, synthesis, and growth mechanisms of carbon nanotubes with special focus on thermal chemical vapor deposition.* Nanoscale, 2010. **2**(8): p. 1306-1323.

30. De Volder, M.F., et al., *Carbon nanotubes: present and future commercial applications.* science, 2013. **339**(6119): p. 535-539.

31. Acomb, J.C., et al., *The use of different metal catalysts for the simultaneous production of carbon nanotubes and hydrogen from pyrolysis of plastic feedstocks.* Applied Catalysis B-Environmental, 2016. **180**: p. 497-510.

32. Papari, S., et al., *Pyrolytic conversion of plastic waste to value-added products and fuels: A review.* Materials, 2021. **14**(10): p. 2586.

33. Sun, K., et al., *Selective production of aromatics from waste plastic pyrolysis by using sewage sludge derived char catalyst.* Journal of Cleaner Production, 2020. **268**: p. 13.

34. Geyer, R., et al., *Production, use, and fate of all plastics ever made.* Science Advances, 2017. **3**(7): p. 5.

35. Phan, H.H., *Biomass-derived carbon as a precursor for bipolar plate in vanadium redox flow battery*. 2021, Newcastle University.

36. Zhang, Y., et al., *Pyrolysis–catalysis of waste plastic using a nickel–stainless-steel mesh catalyst for high-value carbon products.* Environmental technology, 2017. **38**(22): p. 2889-2897.

37. Freel, J. and A.K. Galwey, *Hydrocarbon cracking reactions on nickel.* Journal of Catalysis, 1968. **10**(3): p. 277-289.

38. He, Z., et al., *Iron Catalysts for the Growth of Carbon Nanofibers: Fe, Fe3C or Both?* Chemistry of Materials, 2011. **23**(24): p. 5379-5387.

39. Sun, K., et al., *Effect of ZnCl2-activated biochar on catalytic pyrolysis of mixed waste plastics for producing aromatic-enriched oil.* Waste Management, 2018. **81**: p. 128-137.

40. Miandad, R., et al., *Catalytic pyrolysis of plastic waste: A review*. Process Safety and Environmental Protection, 2016. **102**: p. 822-838.

41. Martínez-Narro, G., et al., *Chemical recycling of mixed plastic waste via catalytic pyrolysis.* Journal of Environmental Chemical Engineering, 2022. **10**(5): p. 108494.

42. Genuino, H.C., et al., *Pyrolysis of mixed plastic waste: Predicting the product yields.* Waste Management, 2023. **156**: p. 208-215.

43. López, A., et al., *Pyrolysis of municipal plastic wastes: Influence of raw material composition.* Waste Management, 2010. **30**(4): p. 620-627.

44. Chang, T., et al., *Effects of temperature zones on pyrolysis products of mixed plastic waste.* Journal of Material Cycles and Waste Management, 2022: p. 1-11.

45. Adrados, A., et al., *Pyrolysis of plastic packaging waste: A comparison of plastic residuals from material recovery facilities with simulated plastic waste.* Waste Management, 2012. **32**(5): p. 826-832.

46. Williams, E.A. and P.T. Williams, *Analysis of products derived from the fast pyrolysis of plastic waste.* Journal of Analytical and Applied Pyrolysis, 1997. **40-41**: p. 347-363.

47. Du, S., et al., *Conversion of polyethylene terephthalate based waste carpet to benzene-rich oils through thermal, catalytic, and catalytic steam pyrolysis.* ACS Sustainable Chemistry & Engineering, 2016. **4**(5): p. 2852-2860.

48. Saad, J.M. and P.T. Williams, *Pyrolysis-catalytic dry (CO2) reforming of waste plastics for syngas production: Influence of process parameters.* Fuel, 2017. **193**: p. 7-14.

49. Gerö, L., *Bond Energies of Hydrocarbons.* The Journal of Chemical Physics, 2004. **16**(11): p. 1011-1013.

50. Boeren, E.G., et al., *Naphtha analysis: The advantages of a specific olefin trap.* Journal of Chromatography A, 1985. **349**(2): p. 377-384.

51. McKee, D.W., *The Kinetics of Propane Cracking on Nickel.* Journal of the American Chemical Society, 1962. **84**(23): p. 4427-4431.

52. Yang, R.-X., et al., *Effects of Nickel Species on Ni/Al2O3 Catalysts in Carbon Nanotube and Hydrogen Production by Waste Plastic Gasification: Bench- and Pilot-Scale Tests.* Energy & Fuels, 2015. **29**(12): p. 8178-8187.

53. Bergman, R.G., *C–H activation.* Nature, 2007. **446**(7134): p. 391-393.

54. Pawelczyk, E., et al., *Pyrolysis Combined with the Dry Reforming of Waste Plastics as a Potential Method for Resource Recovery-A Review of Process Parameters and Catalysts.* Catalysts, 2022. **12**(4).

55. Feng, R., et al., *Direct synthesis of HZSM-5 zeolites with enhanced catalytic performance in the methanol-to-propylene reaction.* Catalysis Today, 2022. **405**: p. 299-308.

56. Le Minh, C., et al., *Carbon–Carbon Bond Cleavage and Dehydrogenation of Isobutane Over HZSM-5 at Low Pressures and Temperatures.* Catalysis letters, 2012. **142**: p. 1470-1473.

57. Trombetta, M., et al., *An FT-IR study of the reactivity of hydrocarbons on the acid sites of HZSM5 zeolite.* Applied Catalysis A: General, 2000. **198**(1-2): p. 81-93.

58. Arabiourrutia, M., et al., *HZSM-5 and HY Zeolite Catalyst Performance in the Pyrolysis of Tires in a Conical Spouted Bed Reactor.* Industrial & Engineering Chemistry Research, 2008. **47**(20): p. 7600-7609.

59. Ratnasari, D.K., et al., *Catalytic pyrolysis of waste plastics using staged catalysis for production of gasoline range hydrocarbon oils.* Journal of Analytical and Applied Pyrolysis, 2017. **124**: p. 631-637.

60. Wong, S.L., et al., *Plastic pyrolysis over HZSM-5 zeolite and fluid catalytic cracking catalyst under ultra-fast heating.* Journal of Analytical and Applied Pyrolysis, 2023. **169**: p. 105793.

61. Miandad, R., et al., *Catalytic pyrolysis of plastic waste: moving toward pyrolysis based biorefineries.* Frontiers in energy research, 2019. **7**: p. 27.

62. Liu, W.-W., et al., *Synthesis of single-walled carbon nanotubes: Effects of active metals, catalyst supports, and metal loading percentage.* Journal of Nanomaterials, 2013. **2013**: p. 63-63.

63. MacKenzie, K.J., et al., *An updated review of synthesis parameters and growth mechanisms for carbon nanotubes in fluidized beds.* Industrial & Engineering Chemistry Research, 2010. **49**(11): p. 5323-5338.

64. Gilbert, P., et al., *Tar reduction in pyrolysis vapours from biomass over a hot char bed.* Bioresource Technology, 2009. **100**(23): p. 6045-6051.

65. Wang, F.J., et al., *Tar reforming using char as catalyst during pyrolysis and gasification of Shengli brown coal.* Journal of Analytical and Applied Pyrolysis, 2014. **105**: p. 269-275.

66. Zhang, Y.L., et al., *Experimental study on pyrolysis tar removal over rice straw char and inner pore structure evolution of char.* Fuel Processing Technology, 2015. **134**: p. 333-344.

67. Business Insider. *Naphtha Price*. 2024; Available from: https://markets.businessinsider.com/commodities/naphthapreis.

68. Businessanalytiq. *Naphtha price index*. 2024; Available from: https://businessanalytiq.com/procurementanalytics/index/naphtha-price-index/.

69. Nanografi. *Short Multi Walled Carbon Nanotubes*. 2024; Available from: https://nanografi.com/carbon-nanotubes/industrial-grade-short-multi-walled-carbon-nanotubes-purity-92-outside-diameter-28-48-nm/.